# PARP14 is pro- and anti-viral host factor that promotes IFN production and affects the replication of multiple viruses

Srivatsan Parthasarathy[1], Pradtahna Saenjamsai[1], Hongping Hao[1], Anna Ferkul[1], Jessica J. Pfannenstiel[1], Ellen L. Suder[2,3,4], Daniel S. Bejan[5], Yating Chen[6], Nancy Schwarting[1], Masanori Aikawa[7,8,9], Elke Muhlberger[2,3,4], Robin C. Orozco[1], Christopher S. Sullivan[6], Michael, S. Cohen[5], David J. Davido[1], Adam J. Hume[2,3,4], Anthony R. Fehr[1*]

[1]Department of Molecular Biosciences, University of Kansas, Lawrence, Kansas 66045, USA
[2]Department of Microbiology, Boston University School of Medicine, Boston, MA, 02118, USA
[3]National Emerging Infectious Diseases Laboratories, Boston University, Boston, MA, 02118, USA
[4]Center for Emerging Infectious Diseases Policy & Research, Boston University, Boston, MA, 02118, USA
[5]Department of Chemical Physiology and Biochemistry, Oregon Health Sciences University, Portland, OR, 97239, USA
[6]Department of Molecular Biosciences, University of Texas, Austin, TX, 78712, USA
[7]Center for Excellence in Vascular Biology (P.K.J., M.A., E.A.), Brigham and Women's Hospital, Harvard Medical School, Boston, MA, 02115, USA.
[8]Center for Interdisciplinary Cardiovascular Sciences (M.A., E.A.), Brigham and Women's Hospital, Harvard Medical School, Boston, MA, 02115, USA.
[9]Channing Division of Network Medicine (M.A.), Brigham and Women's Hospital, Harvard Medical School, Boston, MA, 02115, USA.

*Corresponding author: Dr. Anthony R. Fehr, Molecular Biosciences, University of Kansas, Lawrence, Kansas, USA, Tele: 785-864-6626

Email : arfehr@ku.edu

**Running title :** PARP14 promotes IFN and is a pro- and anti-viral host factor

**Keywords:** ADP-ribosylation, PARP, macrodomain, coronavirus, HSV-1, Ebola virus, Nipah virus, VSV, LCMV, interferon, interferon-stimulated genes,

**ABSTRACT**

PARP14 is a 203 kDa multi-domain protein that is primarily known as an ADP-ribosyltransferase, and is involved in a variety of cellular functions including DNA damage, microglial activation, inflammation, and cancer progression. In addition, PARP14 is upregulated by interferon (IFN), indicating a role in the antiviral response. Furthermore, PARP14 has evolved under positive selection, again indicating that it is involved in host-pathogen conflict. We found that PARP14 is required for increased IFN-I production in response to coronavirus infection lacking ADP-ribosylhydrolase (ARH) activity and poly(I:C), however, whether it has direct antiviral function remains unclear. Here we demonstrate that the catalytic activity of PARP14 enhances IFN-I and IFN-III responses and restricts ARH-deficient murine hepatitis virus (MHV) and severe acute respiratory syndrome coronavirus 2 (SARS-CoV-2) replication. To determine if PARP14's antiviral functions extended beyond CoVs, we tested the ability of herpes simplex virus 1 (HSV-1) and several negative-sense RNA viruses, including vesicular stomatitis virus (VSV), Ebola virus (EBOV), and Nipah virus (NiV), to infect A549 PARP14 knockout (KO) cells. HSV-1 had increased replication in PARP14 KO cells, indicating that PARP14 restricts HSV-1 replication. In contrast, PARP14 was critical for the efficient infection of VSV, EBOV, and NiV, with EBOV infectivity at less than 1% of WT cells. A PARP14 active site inhibitor had no impact on HSV-1 or EBOV infection, indicating that its effect on these viruses was independent of its catalytic activity. These data demonstrate that PARP14 promotes IFN production and has both pro- and anti-viral functions targeting multiple viruses.

## IMPORTANCE

The antiviral response is largely regulated by post-translation modifications (PTM), including ADP-ribosylation. PARP14 is an ADP-ribosyltransferase that is upregulated by interferon and is under positive selection, indicating that it is involved in host-pathogen conflict. However, no anti-viral function has been described for PARP14. Here, we found that PARP14 represses both coronavirus and HSV-1 replication, demonstrating that PARP14 has anti-viral functions. Surprisingly, we also found that PARP14 also has pro-viral functions, as it was critical for the efficient infection of several RNA viruses, including Ebola and Nipah viruses, which have high mortality and are viruses with pandemic potential. These data indicate that PARP14 has both pro- and anti-viral functions and is a potential therapeutic target for highly pathogenic RNA viruses.

## INTRODUCTION

Virus infection causes activation of host immune responses, with the interferon (IFN) response being the major pathway activated. Recognition of viral pathogen-associated molecular patterns (PAMPs) by host surface and cytosolic receptors leads to a series of molecular events that activates the expression of different types of IFNs, that eventually upregulates the expression of anti-viral IFN stimulated genes (ISGs). Several different post-translational modifications regulate this response, including phosphorylation, ubiquitination, and other less common modification such as ADP-ribosylation.

ADP-ribosylation is a post-translational modification (PTM) where ADP-ribose subunits are added to target proteins in a process catalyzed by ADP-ribosyltransferases (ARTs) that use $NAD^+$ as a substrate. The ART Diphtheria toxin-like domain (ARTD) family of ART proteins are intracellular ARTs that are individually named PARPs (1). These ARTDs catalyze the addition of either poly-ADP-ribose (PAR) or mono-ADP-ribose (MAR) to proteins or nucleic acid. The human genome encodes 17 PARPs that are involved in the regulation of most cellular activities including DNA damage repair, ER stress, cell cycle regulation, transcription and translation, and the innate and adaptive immune responses (1). Apart from addition of ADP-ribose, removal of ADP-ribose from target proteins is also implicated in important cellular processes. The presence of ADP-ribose hydrolases (ARH) or macrodomains such as PARG, TARG1, MacroD1 and MacroD2 in humans underscores the importance of ADP-ribose turnover (2).

The expression of several PARPs is activated by IFN in response to virus infection, categorizing them as ISGs. Some PARPs have known antiviral activity including PARP13 (zinc-antiviral protein or ZAP), PARP12, PARP11, PARP9, PARP5a/b, PARP7, and PARP1 (3). In addition,

some PARPs also act as pro-viral factors, promoting viral replication and infection. PARP11 was shown to suppress IFN-I signaling by MARylating IFNAR and priming it for ubiquitination and eventual degradation. The suppression of IFN-I signaling by PARP11 increased the replication of vesicular stomatitis virus (VSV) and herpes simplex virus 1 (HSV-1). These results demonstrated a pro-viral role for PARP11 (4). PARP7-dependent ADP-ribosylation also suppressed IFN-I production and promoted influenza A virus infection, indicating that PARP7 also has pro-viral functions (5). Consistent with this pro-viral function, PARP7 knockdown reduced the replication of murine hepatitis virus (MHV) A59, demonstrating its ability to promote coronavirus replication (6). Finally, PARP1 inhibitors have also been shown to efficiently inhibit replication of several viruses such as herpesviruses, adenoviruses and human immunodeficiency virus (HIV), indicating that PARP1 may also promote virus replication in some cases (7-9).

PARP14 is an ISG that is important in several different biological processes including inflammation, cancer progression and DNA damage. PARP14 is a multidomain protein and its domain architecture was recently re-analyzed using Alphafold2 (10). This analysis determined that PARP14 contains 3 RRM domains, 7 full KH domains and 1 split KH domain that are suspected to bind to nucleic acids, 3 macrodomains (MDs) one of which has an ADP-ribose hydrolase activity (MD1) (10-12), a WWE domain that is suspected to bind ADP-ribose subunits, and the ART catalytic domain (10).

PARP14 was originally identified as a STAT6-binding protein that promoted IL-4 dependent anti-inflammatory signaling (13). Since then, several independent studies have implicated PARP14 in inflammatory and interferon signaling pathways. PARP14's involvement in inflammatory and IFN responses is cell-type and insult dependent, suggesting that PARP14 has

multiple functions that are context dependent. In M1 macrophages PARP14 suppresses IFNγ-induced activation of pro-inflammatory signaling by STAT1 MARylation (14). We and others have found that PARP14 is also critical for inducing high levels of IFN-I following infection with *Salmonella typhimurium*, MHV as well as treatments with LPS or poly(I:C) treatment (6, 15). Specifically, PARP14 knockout M0 macrophages and epithelial cells demonstrated significantly reduced levels of IFN-I after infection or treatment with LPS or poly(I:C), indicating that one of PARP14's functions is to promote IFN-I production, however the mechanisms by which it enhances IFN-I production remain unknown (6, 15).

Interestingly, PARP14 is one of the several PARPs that has evolved under positive selection, indicating that it may be involved in host-pathogen conflicts. This positive selection is seen in many of the different domains of PARP14, especially the macrodomains, WWE domain, and the catalytic domain at the C-terminus of the protein (16). However, despite this evidence for involvement in host-pathogen interactions, there are very few reports describing any impact of PARP14 on virus or bacterial infections. In one report, PARP14 KO RAW264.7 macrophages had significantly increased levels of *S. typhimurium* replication (15). In addition, siRNA knockdown of PARP14 led to a mild increase (~2-fold) in the levels of a Mac1 mutant MHV viral RNA, but knockdown or a congenital knockout of PARP14 did not significantly increase the amount of infectious virus produced (6). Overall, it remains unclear how or if PARP14 impacts virus replication.

Recently, several tools have been developed to facilitate testing the impact of PARP14 on virus infection. First, we reported PARP14 knockout A549 and NHDF cell lines, which have intact IFN systems and are susceptible to infection by a wide variety of viruses. Second, a highly potent and selective PARP14 catalytic inhibitor, RBN01239, was developed (17). Finally, we report

here the creation of a tamoxifen-inducible PARP14 knockout mouse model. Hence, with the availability of an advanced PARP14 inhibitor and with the advent of several PARP14 knock-out systems, we sought to determine the effect of PARP14 and its catalytic activity on IFN production and the replication of multiple different virus families.

Utilizing these tools, we report here that PARP14 influences the replication of multiple viruses. PARP14 potently inhibited the replication of HSV-1 as well as Mac1-mutant MHV and SARS-CoV-2. Unexpectedly, PARP14 also acted as a proviral factor for several negative-sense RNA viruses including vescicular stomatitis virus (VSV), Ebola virus (EBOV), and Nipah virus (NiV), highlighting the multifaceted effect of PARP14 on virus replication. Furthermore, we confirmed that the catalytic activity of PARP14 was critical for IFN induction and the inhibition of CoV replication. This study highlights the involvement of PARP14 in the IFN response and virus infection, underscoring the importance of PARP14 as an immunomodulatory host factor that can affect the replication of multiple viruses.

## RESULTS

### PARP14 promotes IFN-I and IFN-III production in poly(I:C) transfected cells.

We previously demonstrated that PARP14 was required for IFN-I production in response to poly(I:C) in human A549 cells, via an indirect VSV bioassay (6). To determine how PARP14 impacts IFN induction more quantitatively, we induced IFN production via poly(I:C) transfection and quantified the amount of IFNβ and IFNλ transcripts by qPCR and protein by ELISA. Poly(I:C) transfection induced IFNβ **(Fig. 1A)** and IFNλ **(Fig. 1B)** mRNA production in A549 cells, but their levels were significantly reduced in PARP14 knockout (PARP14 KO) compared to wild-type (WT) A549 cells. We also observed a similar decrease in IFNβ and IFNλ protein levels following poly(I:C) transfection in PARP14 KO A549 cells compared to WT cells in an

ELISA assay **(Fig. 1C-D)**. Poly(I:C) transfected PARP14 KO cells also had decreased protein levels of the interferon stimulated gene OAS3 compared to WT cells **(Fig. 1E-F)**. Finally, we also observed a nearly 4-fold reduction in IFN$\beta$ mRNA production in response to poly(I:C) transfection in PARP14 KO NHDF cells we had previously created **(Fig. S1A)** (6). Since PARP14 catalyzes MARylation, we used a highly potent and selective PARP14 catalytic inhibitor, RBN012759 (PARP14i) to test if the observed reduction in IFN and ISG levels were due to the MARylating activity of PARP14. PARP14i efficiently restricted PARP14's auto-MARylation activity in an *in vitro* assay in a dose-dependent manner **(Fig. S1B)**. Importantly, poly(I:C) stimulated A549 cells displayed a dose-dependent decrease in IFNβ transcript levels when treated with PARP14i. At the highest concentration of PARP14i, the level of IFNβ mirrored those in PARP14 KO cells **(Fig. 1G)**. This suggests that the reduction in IFNβ levels in PARP14 KO cells was due to the absence of PARP14 catalytic activity. In addition, we also used a PARP14 degrading compound, RBN012811 (DEG), and its associated negative control, RBN013527 (CTL), to test the role of PARP14 in IFN-I production (a generous gift from Mario Niepel, Ribon Therapeutics) (18). DEG effectively reduced PARP14 protein to undetectable levels in WT A549 cells **(Fig. S1B)**. Compared to CTL, we found that the PARP14 DEG decreased IFN$\beta$ mRNA induction 3-fold, similar to results with complete PARP14 KO cells. Finally, we restored IFNβ transcript abundance to WT levels by exogenously expressing full-length PARP14 in PARP14 KO cells **(Fig. 1H)**, further confirming that the decrease in IFNβ levels in PARP14 KO cells was not due to off-target effects of the PARP14 deletion. These results demonstrate that in response to poly(I:C) stimulation PARP14-dependent MARylation promotes IFN-I and IFN-III production.

**PARP14 promotes IFN-I production in Mac1-mutant CoV infected cells.**

Using congenital PARP14 KO mouse cells, we previously demonstrated that PARP14 was required to promote IFN production upon infection with a Mac1-mutant murine coronavirus (MHV-JHM N1347A) (6). To circumvent the limitations of constitutive PARP14 KO mice, which include poor breeding efficiency and potential confounding effects of developmental compensation for PARP14 KO by other PARPs, we developed a conditional tamoxifen-inducible PARP14 KO mouse model to better identify the role of PARP14 in response to MHV infection **(Fig. 2A)**. *LoxP* sites were inserted into the *parp14* locus around exon 2 via CRISPR mediated mutagenesis to create *parp14* floxed alleles. These mice were then bred with *ert2-cre* heterozygote mice to obtain both *parp14* floxed *ert2-cre* positive mice (*parp14*$^{flox}$*/Ert2-Cre*), and as controls, *parp14* floxed ert2-*cre* negative offspring (*parp14*+/+) **(Fig. 2A)**. BMDMs were harvested from these mice and in *cre* positive cells induction with 4-hydroxy tamoxifen (4-OH-T) led to an efficient knock-out of PARP14 *(parp14-/-)* **(Fig S2A)**. BMDMs that were *cre* negative still expressed PARP14 following treatment with 4-OH-T (*parp14*+/+). MHV-N1347A infection induced robust IFNβ levels compared to WT in *parp14*+/+ BMDMs as previously demonstrated **(Fig. 2B)** (6). However, in *parp14-/-* BMDMs, the level of IFNβ was reduced to *parp14*+/+ BMDM levels, suggesting that PARP14 was required for IFNβ production in response to MHV-N1347A infection, confirming our prior observation and validating our KO mice **(Fig 2B)**. Similarly, there was also a decrease in the induction of ISG15 transcript levels in MHV-N1347A infected cells in *parp14-/-* cells **(Fig S2B)**. To determine if PARP14's ART activity was responsible for the increase in IFN-I expression following infection, MHV-WT and N1347A infected BMDMs were treated with PARP14i and tested for IFNβ mRNA expression. PARP14i treatment caused a dose-dependent decrease in IFNβ expression in BMDMs infected with N1347A **(Fig. 2D)** similar to its impact on poly(I:C) induced IFNβ expression. Following

MHV-N1347A infection, the level of secreted IFNβ protein was also reduced to WT levels in *Parp14-/-* BMDMs and in WT BMDMs treated with PARP14i **(Fig. 2E)**. Previously, we demonstrated that infection with a Mac1 deleted SARS-CoV-2 virus (ΔMac1) induced elevated levels of IFN-I and IFN-III in human epithelial cells, which we hypothesized was due to PARP14 catalytic activity (19). Following ΔMac1 infection of Calu-3 cells, PARP14i treatment of Calu-3 cells reduced the mRNA levels of IFNβ, IFNλ and CXCL10 to levels seen following WT virus infection. These data demonstrate that the increase in IFNβ levels in response to Mac1-deficient human and mouse CoV infection occurs via PARP14-dependent MARylation.

**RNAseq analysis identifies over 100 genes up-regulated by PARP14.**

Next, we used RNAseq to identify all genes that are influenced by PARP14-dependent MARylation, in addition to IFNs and ISGs. To identify PARP14 regulated genes, we analyzed the transcriptome of BMDMs that are infected by N1347A with and without PARP14i **(Fig. 3A)**. As expected from previous studies, N1347A infected DMSO-treated BMDMs had elevated levels of IFN-I, ISGs, and dozens of other genes involved in antiviral immunity. Upon treatment with PARP14i, the mRNA levels of a substantial number of these genes were reduced, indicating that these mRNAs are increased by PARP14-dependent MARylation. Overall, we found that 622 genes were upregulated by PARP14, while 355 genes were downregulated, for a total number of 977 differentially expressed genes expressed above a threshold fold change (FC) of 1.5-fold and threshold P-adjusted value of 0.001 **(Fig. 3A)**. Next, we performed a functional analysis on the genes that are regulated by PARP14 MARylation activity. Most of the genes promoted by PARP14 were genes involved in antiviral immunity **(Fig 3B)**. However, genes involved in apoptosis, transcription, and Ubiquitin ligase conjugation pathway were also upregulated. Representative genes from each of these pathways were validated by qPCR **(Fig. 3C)**. This data

suggests that PARP14 is an important regulator of antiviral immunity but also regulates other cellular processes such as cell death and transcription.

**PARP14 is required for the repression of Mac1-mutant coronavirus replication.**

We previously found that *parp14* knockdown mildly increased the replication of MHV-N1347A in BMDMs, however congenital *parp14* KO mice did not have increased MHV-N1347A replication (6). To determine if PARP14 was required to repress MHV-N1347A, we infected our *parp14-/-* and *parp14+/+* BMDMs as described above. As previously observed, MHV-N1347A had a significant growth defect compared to MHV-WT virus in *parp14+/+* cells, regardless of whether the cells were or were not treated with tamoxifen **(Fig. 4A)**. Interestingly, *parp14-/-* mostly restored the replication of MHV-N1347A, suggesting that PARP14 is required for restricting MHV-N1347A virus replication in BMDMs **(Fig. 4B)**. We also found that MHV-N1347A replication was mostly restored to MHV-WT levels in *parp14-/-* bone-marrow-derived dendritic cells (BMDCs) **(Fig. 4C)**. To test whether this increased MHV-N1347A replication in *parp14-/-* cells is due to PARP14-dependent MARylation, we measured MHV-N1347A replication in the presence and absence of PARP14i. In the presence of PARP14i, N1347A replication was similarly restored to near WT levels, suggesting that the catalytic activity of PARP14 was required for restricting MHV-N1347A replication **(Fig. 4D)**.

We next tested whether PARP14 was required to restrict the replication of severe acute respiratory syndrome coronavirus 2 (SARS-CoV-2) ΔMac1. We previously found that SARS-CoV-2 ΔMac1 replicates near SARS-CoV-2 levels in Calu-3 cells, but that SARS-CoV-2ΔMac1 is more sensitive to IFNγ pre-treatment than WT virus, and IFNγ induces the expression of several PARPs, including PARP14 (19). To determine if PARP14 is required for IFNγ-mediated restriction of SARS-CoV-2ΔMac1, we infected IFNγ-pretreated Calu3 cells with SARS-CoV-2

WT and ΔMac1 with and without PARP14i. Upon treatment with PARP14i, we observed that WT virus was not impacted either in the presence or absence of IFNγ, in contrast, the replication of SARS-CoV-2ΔMac1 in cells pre-treated with IFNγ was significantly increased to levels near that of non-IFNγ treated cells **(Fig. 4E)**. Overall, these results suggest that MARylation triggered by PARP14 is required to restrict the replication of Mac1-deficient MHV and SARS-CoV-2 viruses.

**PARP14 restricts HSV-1 replication.**

PARP14 is one of the PARPs that has evolved under positive selection in primates, indicating that it is involved in host-pathogen conflict (16). Thus, we hypothesized that in addition to CoVs, it might repress the replication of other viral families. First, we tested the effect of PARP14 deletion on HSV-1, which has been co-evolving with humans for several million years. Furthermore, PARP14 was identified as a host factor that binds to HSV-1 DNA (20, 21). We infected A549 WT and two different clones of PARP14 KO cells (6) with HSV-1 (strain KOS) at a low MOI (0.01PFU/mL) and found that replication of HSV-1 was enhanced by over 2-logs throughout the infection in PARP14 KO cells, strongly indicating that PARP14 represses HSV-1 replication **(Fig.5A)**. As a separate measure of replication, we infected WT and KO cells with 0.1 MOI HSV-1 and quantified the expression of ICP0, ICP4 and ICP27 mRNA transcripts at 24 hpi. We observed increased gene expression in PARP14 KO cells compared to WT cells, again indicating that PARP14 restricts HSV-1 infection **(Fig. 5B).** We then corroborated this observation by quantifying ICP0, ICP4 and ICP27 mRNA levels in A549 cells infected with HSV-1 and treated with PARP14 degron (DEG) or its corresponding negative control (CTL). Again, we saw an increase in the transcripts in DEG treated cells, confirming that the observed increase in expression of ICP genes was due to the absence of PARP14 **(Fig. S3)**.

Next, we tested the ability of HSV-1 to form plaques on A549 WT and PARP14 KO cells using a plaquing efficiency assay. Similar to previous observations, we found that PARP14 KO also enhanced the plaquing efficiency of HSV-1 compared to WT cells by >2-logs on average **(Fig. 5C)**. Since the MARylating activity of PARP14 was responsible for restricting CoV replication, we expected that PARP14-dependent MARylation was responsible for the observed restriction of HSV-1 replication, so we tested the ability of PARP14i to enhance HSV-1 infection. Interestingly, HSV-1 replication was not affected in PARP14i treated A549 cells compared to untreated cells, suggesting that PARP14 restricted HSV-1 replication in a MARylation-independent manner **(Fig. 5D)**. Overall, these data show that PARP14 restricts HSV-1 infection and does so in an ADP-ribosylation independent manner.

**PARP14 promotes the replication of several negative-sense RNA viruses.**

Next, we tested the ability of PARP14 to restrict the replication of additional types of RNA viruses. First, we tested the infectivity of lymphocytic choriomengingitis virus Clone-13 (LCMV-cl13), an ambisense RNA virus, in WT and PARP14 KO BMDMs. To measure infectivity of LCMV-cl13 in BMDMs, we measured the amount of LCMV nucleoprotein (LCMV-NP) using a fluorescently labeled antibody against LCMV-NP (clone anti-VL4) and intracellular flow cytometry. PARP14 KO cells had comparable levels of LCMV-NP+ cells compared to WT cell, ~4-5%. These data indicate that LCMV-cl13 infection is not impacted by PARP14 (Fig. S4A-B). To further explore the role of PARP14 in the replication of negative-sense RNA viruses, we tested the ability of vesicular stomatitis virus (VSV), Ebola virus (EBOV), and Nipah virus (NiV) to infect PARP14 KO A549 cells. Interestingly, VSV-GFP replication was significantly reduced by ~5-fold in A549 PARP14 KO cells compared to WT cells, indicating that PARP14 promotes VSV-GFP replication **(Fig. 6A)**. An even more

remarkable effect was observed following infection of PARP14 KO cells with EBOV-ZsGreen and NiV. While WT A549 cells infected with EBOV-ZsGreen demonstrated robust infection, indicated by GFP expression, A549 PARP14 KO cells were dramatically less infected **(Fig. 6B)**. Quantitation of the number of infected cells showed that the infectivity rate for EBOV-ZsGreen in A549 PARP14 KO cells was less than 1% compared to WT cells **(Fig. 6C)**. suggesting that PARP14 was critical for EBOV replication. Similarly, when we tested the infectivity of NiV in A549 cells, there was a substantial decrease in virus infectivity in PARP14 KO cells, with an infectivity rate less than 10% compared to WT cells **(Fig. 6D)**. We next tested whether the ADP-ribosyltransferase activity of PARP14 supported VSV, EBOV-ZsGreen or NiV infectivity by treating A549 WT cells with PARP14i. PARP14i treatment did not significantly reduce either VSV replication or EBOV-ZsGreen infectivity, and only mildly reduced NiV infectivity, indicating that the proviral function of PARP14 was largely independent of its MARylating activity **(Fig. 6E-G)**. Overall, these results suggest that PARP14 can inhibit the replication of CoVs and HSV-1, but also acts as a critical pro-viral factor for multiple negative-sense RNA viruses.

## DISCUSSION

PARP14 has emerged as a critical host factor that impacts multiple immune signaling pathways. It was initially found to bind STAT6 and promote IL4-dependent anti-inflammatory gene regulation (13). This function of PARP14 promotes $T_H2$ gene expression and IgE production in immune cells (22). Recently, a PARP14 inhibitor (RBN-3143) was reported to mitigate the effects of allergen-induced IgE production and overproduction of mucus, reduced $T_H2$ cell abundance and restored $\alpha$PD-1 sensitivity to tumors (23). PARP14 also inhibits STAT-1 phosphorylation by MARylating key residues, and knockdown or knockout of PARP14

increased pro-inflammatory cytokines in primary human and mouse M1, but not M2 macrophages (14). In contrast, PARP14 promoted IFN-I and pro-inflammatory cytokine production in RAW 264.7 cells following LPS treatment and *S. typhimurium* infection (15). PARP14 also promoted IFN-I production in response to MHV infection and poly(I:C) stimulation in BMDMs and A549 cells, respectively (6). In this study, we demonstrated that the enzymatic activity of PARP14 promotes IFN-I and IFN-III production when stimulated with a dsRNA analog poly(I:C) or CoV infection by directly quantifying IFN-I and IFN-III mRNA and protein levels in multiple cell lines. In general, the impact of PARP14 on innate and adaptive immune pathways is cell type and condition specific. It remains unclear if PARP14 both enhances IFN-I and IFN-III production and limits IFN signaling in the same cells, or if it only represses IFN signaling in M1 macrophages. It is feasible that PARP14 may dampen IFN signaling to control its own ability to stimulate IFN production. How PARP14 regulates IFN production and signaling and the broader impacts of these functions remains unclear and is an active topic of research.

PARP14 is one of 4 PARPs that has evolved under positive selection, indicating that it is likely involved in host-pathogen conflict (16). Furthermore, PARP14 is stimulated by IFNs and virus infections (6). Despite this, there is very limited evidence that PARP14 inhibits or promotes virus infection. Here, we show the effect of PARP14 in multiple virus infections. PARP14 was required to repress the replication of a Mac1-mutant MHV, N1347A, SARS-CoV-2 ΔMac1, and surprisingly a DNA virus, HSV-1. Either of these findings could explain the positive selection of PARP14. All CoVs encode for the highly conserved Mac1 domain, indicating that countering PARP activity, including PARP14, was critical for their survival (19, 24). Thus, PARP14 may have evolved with Mac1, though since Mac1 appears to fully counter Mac1, this seems unlikely.

In contrast, HSV-1 and other herpesviruses have been evolving with mammals for millions of years, so it is maybe more likely that PARP14 is co-evolving with herpesviruses. Finally, we found that PARP14 is critical for the replication of several negative sense RNA viruses including VSV, EBOV and NiV, though largely in an ADP-ribosylation independent manner. PARP14 has been shown to interact with SARS-CoV-2 RNA (25), HSV-1 DNA (20), and in a separate context complexes with PARP9 and the E3 ubiquitin ligase, DTX3L (26). PARP9 and DTX3L were shown to target the encephalomyocarditis virus (EMCV) 3C protease for degradation (27). However, it is yet unclear if the interaction of PARP14 with these factors impacts virus replication. It will be of great interest to identify protein and/or nucleic acid binding partners of PARP14 during infection and define the mechanisms by which it both inhibits and promotes virus replication.

PARP14 is a large protein (203kDa) with multiple domains (10). The ADP-ribosyl transferase (ART) domain of PARP14 binds to $NAD^+$ and transfers an ADP-ribose moiety to its targets. Its ART domain has an HYL (hydrophobic residue-tyrosine-leucine) domain as part of the catalytic triad, which restricts its ART activity to MARylation (28, 29). PARP14 also has 3 tandem macrodomains (MD), of which MD1 has ADP-ribosylhydrolase (ARH) activity against MARylated protein and nucleic acid substrates, making it a rare enzyme that both adds and reverses the same post-translational modification (11, 12). PARP14 also has a WWE domain that can bind to ADP-ribose subunits (30), several KH domains that facilitate protein and nucleic acid binding, and several RNA recognition motifs (RRMs) (10). However, the roles and substrates of these domains, especially during virus infection, remain largely unknown. While PARP14 promotes IFN production and restricts CoV replication in an ADPr-dependent manner, it also influenced the replication of multiple virus infections in an ADPr-independent fashion (HSV-1,

EBOV). Recently, PARP14 was also seen to bind to the HSV-1 genome, in association with other DNA repair proteins as early as 3 hours post-infection, suggesting that PARP14 possibly binds to DNA to inhibit transcription and/or DNA replication (20, 21). Given the potential of PARP14 to bind and alter protein and nucleic acid substrates through its many domains, identifying the domains that impact virus infection could reveal several novel mechanisms by which PARP14 regulates virus replication and pathogenesis. As PARP14 is critical for the replication of several negative-sense RNA viruses of high pandemic potential (EBOV and NiV), developing inhibitors targeting the domains that are required for their replication could prove to be an effective strategy for mitigating outbreaks of multiple highly pathogenic negative-sense RNA viruses.

## MATERIALS AND METHODS

### Biosafety statements

All work with SARS-CoV-2 was conducted in the University of Kansas EHS-approved BSL-3 facility following standard operating procedures. All work with wild-type and recombinant Ebola virus and Nipah virus was performed in the biosafety level 4 (BSL-4) facility of Boston University's National Emerging Infectious Diseases Laboratories (NEIDL) following approved standard operating procedures in compliance with local and national regulations pertaining to handling BSL-4 pathogens and Select Agents. Animal studies were approved by the Institutional Animal Care and Use Committees at the University of Iowa and the University of Kansas and met stipulations of the Guide for the Care and Use of Laboratory Animals.

### Cell culture and reagents

NHDF, 293T, Hela-MVR, A549, A549-PARP14KO, A549-ACE2 (a generous gift from Susan Weiss, University of Pennsylvania), BHK, 17Cl-1, and Vero E6 cells were grown in Dulbecco's modified Eagle medium (DMEM) supplemented with 10% fetal bovine serum (FBS). Calu-3 cells (ATCC) were grown in MEM supplemented with 20% FBS. Baby hamster kidney cell line BSR-T7/5 constitutively expressing T7 RNA polymerase was maintained in Glasgow's Minimum Essential Medium (G-MEM) with 10% FBS. Bone marrow derived cells were grown in RPMI supplemented with 10% FBS and differentiated into M0 macrophages using M-CSF (Millipore-Sigma) and dendritic cells (DCs) using GM-CSF (Millipore-Sigma). All cell lines were grown at 37□ and 5% $CO_2$. IFN-$\gamma$ was purchased from R&D Systems and Poly(I:C) HMW (0.5μg/mL) was purchased from Millipore-Sigma. RBN012759 (PARP14i) was purchased from Atomwise. RBN012811 (DEG) and its associated negative control RBN013527 (CTL) were generously provided by Dr. Mario Niepel (Ribon Therapeutics). Cells were transfected with

either Polyjet (Amgen), Lipofectamine 3000 (Fisher Scientific), or jetOPTIMUS (Polyplus) per the manufacturer's instructions.

**Creation of inducible PARP14 knock-out mice**

*Animals.* The insertion of loxP sites flanking exon 2 of PARP14 was carried out by the University of Iowa genome editing facility. C57BL/6J mice were purchased from Jackson Labs (000664; Bar Harbor, ME). Male mice older than 8 weeks were used to breed with 3-5-week-old super-ovulated females to produce zygotes for pronuclear injection. Female ICR (Envigo; Hsc:ICR(CD-1)) mice were used as recipients for embryo transfer. All animals were maintained in a climate-controlled environment at 25□ and a 12/12 light/dark cycle.

*Preparation of Cas9 RNPs and the injection mix.* Chemically modified CRISPR-Cas9 crRNAs targeting regions 5' and 3' of exon 2 of PARP14 **(Table S1)** and CRISPR-Cas9 tracrRNA were purchased from IDT (Alt-R® CRISPR-Cas9 crRNA; Alt-R® CRISPR-Cas9 tracrRNA (Cat# 1072532)). The crRNAs and tracrRNA were suspended in T10E0.1 and combined to 1 ug/ul (~29.5 uM) final concentration in a 1:2 (µg:µg) ratio. The RNAs were heated at 98□ for 2 min and allowed to cool slowly to 20□ in a thermal cycler. The annealed cr:tracrRNAs were aliquoted to single-use tubes and stored at -80□. Cas9 nuclease was also purchased from IDT (Alt-R® S.p. HiFi Cas9 Nuclease). Cr:tracr:Cas9 ribonucleoprotein complexes were made by combining Cas9 protein and cr:tracrRNA in T10E0.1 (final concentrations: 250 ng/$\mu$l (~1.6 $\mu$M) Cas9 protein and 200 ng/$\mu$l (~6.1 $\mu$M) cr:tracrRNA). The Cas9 protein and annealed RNAs were incubated at 37□ for 10 minutes. The RNP complexes were combined with single-stranded repair template, containing the loxP sites to be inserted around exon2, and incubated an additional 5 minutes at 37□ (single-stranded repair template sequence available upon request).

The concentrations in the injection mix were 50 ng/$\mu$l (~0.3 $\mu$M) Cas9 protein and 20 ng/$\mu$l (~0.6 $\mu$M) each cr:tracrRNA and 40 ng/$\mu$l single-stranded repair template.

*Collection of embryos and injection.* Pronuclear-stage embryos were collected using methods described in (31). Embryos were collected in KSOM media (Millipore; MR101D) and washed 3 times to remove cumulous cells. Cas9 RNPs and double-stranded repair template were injected into the pronuclei of the collected zygotes and incubated in KSOM with amino acids at 37□ under 5% $CO_2$ until all zygotes were injected. The CRISPR injection protocol was previously described(32). Fifteen to 25 embryos were immediately implanted into the oviducts of pseudo-pregnant ICR females. Offspring were heterozygote for the loxP insertions. These mice were sequentially bred to result in floxed homozygote mice. Genotyping was performed using PCR amplification with primers listed in **Table S2**. and restriction digestion by EcoR1. These were then crossed with C57BL/6.Cg-Ndor1$^{Tg(UBC\text{-}cre/ERT2)1Ejb}$/IJ mice (Jax strain # 007001) till mice colonies that were homozygous for *loxP* sites and heterozygous for *cre* gene were confirmed by genotyping. The resulting mice were backcrossed twice before using these mice for the experiments described in this study.

**Virus infections**

*MHV-JHM$^{IA}$*. Recombinant WT and N1347A MHV JHM$^{IA}$ virus used in this study have been previously reported (6, 33, 34). Virus stocks were grown in 17Cl-1 cells and titered by plaque assay in Hela-MVR cells. BMDMs and DCs were infected at an MOI of 0.1 PFU/cell for indicated periods of times after a 60-min adsorption phase. Virus titers were determined by plaque assay on Hela-MVR cells.

*SARS-CoV-2*. Recombinant SARS-CoV-2 WT and ΔMac1 virus based on the original Wuhan isolate used in this study has been previously reported (19). Virus stocks were grown and titered

by plaque assay in VeroE6 cells. A549-ACE2 cells were infected at an MOI of 0.1 for 48 hours after a 60-min adsorption phase. Calu3 cells were infected at an MOI of 0.1 for 48 hours after a 120-min adsorption phase and Trypsin-TCPK treatment (1μg/mL). Virus titers were determined in Vero E6 cells using plaque assay. All the SARS-CoV-2 experiments were carried out under BSL-3 conditions at the University of Kansas, following approved SOPs.

*HSV-1*. Stocks of HSV-1 strain KOS was propagated and titered as previously described (35). For viral yield assays, A549 and A549-PARP14KO cells ($5\times10^4$) were seeded in triplicate in a 24-well plate and infected at an MOI of 0.1 PFU/cell with HSV-1. At 1 hpi, cells were washed twice with PBS to remove unabsorbed virus. Infected cells were harvested and collected 24 hpi and titered by standard plaque assays on Vero cells. For PARP14 inhibitor experiments, A549 cells were treated with or without PARP14 inhibitor, and infections were carried out as described for the HSV-1 yield assays. To determine plaquing efficiencies, A549 and A549-PARP14KO cells were plated in triplicate in 12-well plates and infected with serial dilutions from HSV-1 stocks, and titers were determined by standard plaque assays. To assess virus transcript levels, A549 cell lines ($5\times10^4$) were plated in triplicate in a 24-well plate. Cells were infected at an MOI of 0.1 with HSV-1 and washed twice with PBS 1 hpi. At 6 hpi, media were removed, and cells were resuspended in TRIzol reagent (250 μL). RNA was isolated according to manufacturer's protocol and reverse transcribed as published (ref). cDNAs of viral and cellular transcripts were amplified using primers for ICP0, ICP4, ICP27, and 18S rRNA as previously described (36).

*VSV*. VSV-GFP Indiana strain was generously provided by Dr. Asit Pattnaik (University of Nebraska-Lincoln) (37). Virus stocks were grown and titered by plaque assay in VeroE6 cells. A549 cells were infected with VSV-GFP at an MOI of 1 PFU/cell. Infected cells were then

incubated and collected at 10 hpi after a 60-min adsorption phase. Virus titer was determined by 50% tissue culture infectious dose ($TCID_{50}$) assay in Vero E6 cells.

*LCMV*. LCMV Clone-13 (LCMV-cl13) virus stocks were grown in BHK cells and titered by plaque assay in Vero E6 cells. BMDM cells were infected with LCMV-cl13 at an MOI of 2-6. Infected cells were then incubated and collected at 24 hpi. For surface staining, samples were treated with Fc block (CD16/32, eBioscience) and then incubated with Tonbo Ghost Viability dye (violet 510, Tonbo biosciences), F4/80 (Pacific orange, Invitrogen, CLONE) and LCMV-NP (clone VL4 (BioXcell), self-conjugated to Alexa Fluor 488 following manufacturer's instructions, (Thermo Fisher Scientific)). All flow cytometry data were analyzed using FlowJo software (BD Biosciences).

*EBOV AND NiV*. NiV Bangladesh isolate (NiV-B) was kindly provided by H. Feldmann, NIH NIAID Rocky Mountain laboratories. rEBOV-ZsG-P2A-VP40 (38) and NiV-B stocks were grown in Vero E6 cells as previously described (39). Virus titers were determined in Vero E6 cells by $TCID_{50}$. All work with EBOV-ZsG and NiV-B was performed under BSL-4 conditions at the NEIDL, following approved SOPs. WT and PARP14 knockout A549 cells (clones C2 and C23) were seeded at $2\times10^4$ cells/well in a 96 well plate in DMEM containing 2% FBS. The next day, cells were either mock infected or infected with rEBOV-ZsG-P2A-VP40 (rEBOV-ZsG) or wild-type NiV-B at an MOI of 10. Cells were fixed at 2 dpi in 10% formalin (Fisher Scientific) for at least 6 hours.

**Immunoblotting**

Total cell extracts were lysed in sample buffer containing SDS, protease and phosphatase inhibitors (Roche), $\beta$-mercaptoethanol, and a universal nuclease (Fisher Scientific) and boiled at 95ºC for 5 minutes. Proteins were resolved on an SDS polyacrylamide gel, transferred to a

polyvinylidene difluoride (PVDF) membrane, hybridized with a primary antibody, reacted with an infrared (IR) dye-conjugated secondary antibody, visualized using a Li-COR Odyssey Imager (Li-COR), and analyzed using Image Studio software. Primary antibodies used for immunoblotting included anti-SARS-CoV-2 N (SinoBiological 40143-R001, 1:5000), anti-OAS3 (Cell Signaling 41440, 1:250), anti-PARP14 (Santa Cruz Biotechnology SC-377150, 1:100), and anti-GAPDH (Millipore-Sigma G8795, 1:5000) antibodies. Secondary IR antibodies were purchased from Li-COR.

**PARP14 cellular ADP-ribosylation assays**

293T cells were transfected with GFP-PARP14 WT or GFP-PARP14 G832E plasmid using the jetOPTIMUS transfection reagent with 0.4 µg DNA/well and with a ratio of 1:1 µL transfection reagent: µg DNA. The media was exchanged 4 hours post-transfection. The next day, cells were dosed with RBN012759 for 4 hours. Cells were washed once with cold PBS and the plate was frozen at -80ºC prior to lysis. Samples were thawed on ice, lysed with a cytosolic lysis buffer [50 mM HEPES pH 7.4, 150 mM NaCl, 1 mM $MgCl_2$, 1% tritonX-100 supplemented with fresh 1 mM TCEP, 1X cOmplete EDTA-free Protease Inhibitor Cocktail (Roche) and 30 µM Phthal01 (panPARP inhibitor) (40)], and clarified by centrifugation at 14,000 rpm at 4ºC for 10 minutes. The supernatant containing total protein was quantified using the Bradford assay reagent (Bio-Rad). Lysates were normalized and sample buffer was added to 1X (10% glycerol, 50mM Tris-Cl (pH 6.8), 2% SDS, 1% β-mercaptoethanol, 0.02% bromophenol blue). Samples were boiled at 95ºC for 5 min and resolved in 4-20% Mini-PROTEAN® TGX™ Precast Protein Gels (Bio-Rad). Proteins were transferred to a nitrocellulose membrane and probed overnight at 4ºC with primary antibodies, followed by incubation with goat anti-rabbit (1:10000, Jackson Immuno Reseach Labs) or goat anti-mouse (1:5000, Invitrogen) HRP-conjugated secondary antibodies.

The blots were then incubated SuperSignal™ West Pico substrate (Thermo Scientific) and imaged on a ChemiDoc Gel Imaging System (Bio-Rad). Primary antibodies used for this experiment were: Poly/Mono-ADP ribose antibody (Cell Signaling Technology, E6F6A, 1:2000), Tubulin (Cell Signaling Technology, DM1A, 1:2000), GFP (Proteintech, pabg1, 1:1000), Mono-ADP-Ribose antibody 33204 (Bio-Rad, HCA354, 2 µg/ml), and PARP14 (Millipore Sigma, HPA012063, 1:1000).

**Real-Time (RT-qPCR) Analysis**

RNA was isolated from respective cells using Trizol (Invitrogen). Briefly, cells were collected at indicated time points in Trizol (Invitrogen) and RNA was isolated as per manufacturer's instructions. cDNA was prepared using M-MuLV-reverse transcriptase per the manufacturer's instructions (NEB). qPCR was performed using PowerUp SYBR green master mix (Applied Biosystems) and primers listed in **Table S3**. Cycle threshold values were normalized to hypoxanthine phosphoribosyltransferase (HPRT), glyceraldehyde-3-phosphate dehydrogenase (GAPDH), or 18S rRNA levels using the ΔCt method.

**RNAseq**

RNA was isolated from infected BMDMs with and without treatment, isolated from C57BL6 mice as described above. Library preparation with indexing was performed by the University of Kansas Genome Sequencing core facility with NEB Next RNA Library kit (NEB). RNAseq was performed using an Illumina NextSeq2000 high-output system with paired-end reads of 50 bp. DESeq2 was used to identify DEGs between the BMDM without treatment and MHV-JHM N1347A infected and BMDM with 100nM PARP14 inhibitor treatment and N1347A infected samples using simply "treatment" as a factor. DEGs were identified based on the false-discovery rate corrected *P*-value ($P_{ADJ}$) and $\log_2$-fold-change of ($\log_2$FC) between the samples. Genes were

considered up-regulated in an MHV-JHM-infected sample if $P_{ADJ} < 0.05$ and $\log_2FC > 0.6$, which is nearly equivalent to a 1.5-fold increase. Similarly, genes were considered down-regulated if $P_{ADJ} < 0.05$ and $\log_2FC < -0.6$, or a 1.5-fold decrease. DEGs were subjected to gene ontology analysis using the Database for Annotation, Visualization and Integrated Discovery (DAVID: https://david.ncifcrf.gov/).

**Primers**

Primers were used at 10μM concentration and the primers sequences for human HPRT, IFNβ, GAPDH (41), CXCL10 and mouse HPRT, IFNβ and ISG15 have been previously published (19). RNAseq data was corroborated by qPCR using primer sequences CASP1F TACACGTCTTGCCCTCATTATC, CASP1R CTCCAGCAGCAACTTCATTTC, FOXO3F TTTCCTACGTCTCCTGCTAATG, FOXO3R CTCCTTAGGCTGACGCTAATC, RNF111F CGACTTCATCACCTCCAGTTAG, RNF111R GCTCCATCCAATCCTGAAGAA. Dentritic cell verification was done using qPCR using the primers CXCR1F TTCCCATCTGCTCAGGACCTC and CXCR1R ATTTCCCACCAGACCGAACG.

**Immunofluorescence Analysis and Imaging**

Immunofluorescence to detect NiV was performed as described as follows. Briefly, formalin-fixed cells were washed 4 times with phosphate-buffered saline (PBS), permeabilized with a mixture of acetone and methanol (1:1, *v*/*v*) for 5 min at −20 °C, washed 4 times with PBS, treated with 0.1 M glycine for 5 min at room temperature, washed 4 times with PBS, and then incubated in blocking solution (2% bovine serum albumin, 0.2% Tween 20, 3% glycerol, and 0.05% sodium azide in PBS) for 1 h at room temperature. The primary antibody used for the detection of NiV (mouse hyperimmune ascitic fluid diluted 1:500 in blocking solution, BEI NR-48961) was added and incubated overnight at 4°C. Cells were washed 4 times with PBS and then

incubated with secondary antibody (goat α-mouse AlexaFluor 488 diluted 1:100 in blocking solution, Invitrogen) in the presence of 4′,6-diamidino-2-phenylindole (DAPI; 200 ng/mL). rEBOV-ZsG-infected cells were stained with DAPI (200 ng/mL). Infections and immunofluorescence analyses were performed three times in independent experiments.

Samples were imaged at 4x magnification on a Nikon Ti2 Eclipse inverted fluorescent microscope and Photometrics Prime BSI camera using NIS Elements AR software. One representative image from each well, covering an area of 10.87 $mm^2$, was collected for quantification.

**Quantification from images**

Quantification of immunofluorescence and DAPI-stained samples was performed using QuPath software for quantitative pathology. Samples were analyzed with the Positive Cell Detection function of QuPath (42), using DAPI staining to detect cells and ZsGreen fluorescence (rEBOV-ZsG-P2A-VP40) or AF488 staining (NiV-B) intensity in the area surrounding each detected nucleus to identify positive cells, generating infected percentages of total cell numbers. Workflow groovy scripts from each quantification method are available upon request.

**Statistics.** A Student's *t* test or one-way ANOVA were used to analyze differences in mean values between groups. All results are expressed as means ± standard errors of the means (SEM). P values of ≤0.05 were considered statistically significant (*, P≤0.05; **, P≤0.01; ***, P≤0.001; ****, P ≤0.0001; n.s., not significant).

**Data and materials availability.** All the RNAseq reads data will be deposited in NCBI and will be made public upon publication or August 1, 2024, whichever comes first.

## ACKNOWLEDGMENTS

We thank members of the Davido and Orozco labs for valuable discussion. We thank Stanley Perlman, Susan Weiss, Mario Niepel, Asit Pattnaik, and Heinz Feldmann for reagents. Bioinformatic consultation was provided by the KU Center for Genomics. Research reported in this publication was made possible in part by the services of the KU Genome Sequencing Core which is supported by NIH/NIGMS under grant award number P30GM145499, and the KU Flow Cytometry Core, which is supported in part by the NIH/NIGMS under grant award number P20GM113117. Transgenic mice were generated at the University of Iowa Genome Editing Core Facility directed by William Paradee, PhD and supported in part by grants from the NIH and from the Roy J. and Lucille A. Carver College of Medicine. We wish to thank Norma Sinclair, Patricia Yarolem, Joanne Schwarting and Rongbin Guan for their technical expertise in generating transgenic mice. We also thank Mitchell White (Boston University) for excellent technical assistance.

**Funding:**
National Institutes of Health (NIH) grant P20GM113117 (ARF & RCO)
National Institutes of Health (NIH) grant K22AI134993 (ARF)
National Institutes of Health (NIH) grant R35GM138029 (ARF)
National Institutes of Health (NIH) grant R01AI123231 (CSS)
National Institutes of Health (NIH) grant R01HL126901 (MA)
National Institutes of Health (NIH) grant R01AI133486 (EM)
National Institutes of Health (NIH) grant R21AI169646 (EM)
National Institutes of Health (NIH) grant UC7 AI070088 (EM)
Bill & Melinda Gates Foundation grant INV-048926 (EM)

**Author contributions:**
Conceptualization: SP, ARF
Methodology: SP, ELS, DSB, NS, MA, RCO, CSS, MSC, DJD, AJH, ARF
Investigation: SP, PS, HH, AF, JJP, ELS, DSB, YC, NS, RCO, CSS, DJD, AJH, ARF
Visualization: SP, PS, HH, AF, JJP, ELS, DSB, YC, RCO, CSS, MSC, DJD, AJH, ARF
Supervision: SP, EM, RCO, CSS, MSC, DJD, AJH, ARF
Writing—original draft: SP, ARF
Writing—review & editing: SP, PS, HH, AF, JJP, ELS, DSB, YC, NS, JA, EM, RCO, CSS, MSC, DJD, AJH, ARF

**Competing interests:** ARF is in the process of submitting a patent application for use of SARS-CoV-2 ΔMac1 virus as a live-attenuated vaccine.

## REFERENCES


1. B. Luscher *et al.*, ADP-ribosyltransferases, an update on function and nomenclature. *FEBS J* **289**, 7399-7410 (2022).
2. J. G. Rack, D. Perina, I. Ahel, Macrodomains: Structure, Function, Evolution, and Catalytic Activities. *Annu Rev Biochem* **85**, 431-454 (2016).
3. P. N. Brady, A. Goel, M. A. Johnson, Correction for Brady et al., "Poly(ADP-Ribose) Polymerases in Host-Pathogen Interactions, Inflammation, and Immunity". *Microbiol Mol Biol Rev* **83** (2019).
4. T. Guo *et al.*, ADP-ribosyltransferase PARP11 modulates the interferon antiviral response by mono-ADP-ribosylating the ubiquitin E3 ligase beta-TrCP. *Nat Microbiol* **4**, 1872-1884 (2019).
5. T. Yamada *et al.*, Constitutive aryl hydrocarbon receptor signaling constrains type I interferon-mediated antiviral innate defense. *Nat Immunol* **17**, 687-694 (2016).
6. M. E. Grunewald *et al.*, The coronavirus macrodomain is required to prevent PARP-mediated inhibition of virus replication and enhancement of IFN expression. *PLoS Pathog* **15**, e1007756 (2019).
7. S. L. Grady, J. Hwang, L. Vastag, J. D. Rabinowitz, T. Shenk, Herpes simplex virus 1 infection activates poly(ADP-ribose) polymerase and triggers the degradation of poly(ADP-ribose) glycohydrolase. *J Virol* **86**, 8259-8268 (2012).
8. H. C. Ha *et al.*, Poly(ADP-ribose) polymerase-1 is required for efficient HIV-1 integration. *Proc Natl Acad Sci U S A* **98**, 3364-3368 (2001).
9. I. Tempera *et al.*, Regulation of Epstein-Barr virus OriP replication by poly(ADP-ribose) polymerase 1. *J Virol* **84**, 4988-4997 (2010).
10. M. J. Suskiewicz *et al.*, Updated protein domain annotation of the PARP protein family sheds new light on biological function. *Nucleic Acids Res* **51**, 8217-8236 (2023).
11. S. E. Delgado-Rodriguez, A. P. Ryan, M. D. Daugherty, Recurrent Loss of Macrodomain Activity in Host Immunity and Viral Proteins. *Pathogens* **12** (2023).
12. N. Dukic *et al.*, PARP14 is a PARP with both ADP-ribosyl transferase and hydrolase activities. *Sci Adv* **9**, eadi2687 (2023).
13. S. Goenka, M. Boothby, Selective potentiation of Stat-dependent gene expression by collaborator of Stat6 (CoaSt6), a transcriptional cofactor. *Proc Natl Acad Sci U S A* **103**, 4210-4215 (2006).
14. H. Iwata *et al.*, PARP9 and PARP14 cross-regulate macrophage activation via STAT1 ADP-ribosylation. *Nat Commun* **7**, 12849 (2016).
15. G. Caprara *et al.*, PARP14 Controls the Nuclear Accumulation of a Subset of Type I IFN-Inducible Proteins. *J Immunol* **200**, 2439-2454 (2018).
16. M. D. Daugherty, J. M. Young, J. A. Kerns, H. S. Malik, Rapid evolution of PARP genes suggests a broad role for ADP-ribosylation in host-virus conflicts. *PLoS Genet* **10**, e1004403 (2014).
17. L. B. Schenkel *et al.*, A potent and selective PARP14 inhibitor decreases protumor macrophage gene expression and elicits inflammatory responses in tumor explants. *Cell Chem Biol* **28**, 1158-1168 e1113 (2021).
18. T. J. Wigle *et al.*, Targeted Degradation of PARP14 Using a Heterobifunctional Small Molecule. *Chembiochem* **22**, 2107-2110 (2021).
19. Y. M. Alhammad *et al.*, SARS-CoV-2 Mac1 is required for IFN antagonism and efficient virus replication in cell culture and in mice. *Proc Natl Acad Sci U S A* **120**, e2302083120 (2023).
20. J. A. Dembowski, N. A. DeLuca, Temporal Viral Genome-Protein Interactions Define Distinct Stages of Productive Herpesviral Infection. *mBio* **9** (2018).

663 21. J. A. Dembowski, S. E. Dremel, N. A. DeLuca, Replication-Coupled Recruitment of Viral and
664 Cellular Factors to Herpes Simplex Virus Type 1 Replication Forks for the Maintenance and
665 Expression of Viral Genomes. *PLoS Pathog* **13**, e1006166 (2017).
666 22. S. Goenka, S. H. Cho, M. Boothby, Collaborator of Stat6 (CoaSt6)-associated poly(ADP-ribose)
667 polymerase activity modulates Stat6-dependent gene transcription. *J Biol Chem* **282**, 18732-
668 18739 (2007).
669 23. C. W. Wong *et al.*, PARP14 inhibition restores PD-1 immune checkpoint inhibitor response
670 following IFNgamma-driven acquired resistance in preclinical cancer models. *Nat Commun* **14**,
671 5983 (2023).
672 24. Y. M. O. Alhammad *et al.*, The SARS-CoV-2 Conserved Macrodomain Is a Mono-ADP-
673 Ribosylhydrolase. *J Virol* **95** (2021).
674 25. I. T. Whitworth *et al.*, Defining Distinct RNA-Protein Interactomes of SARS-CoV-2 Genomic and
675 Subgenomic RNAs. *J Proteome Res* **23**, 149-160 (2024).
676 26. H. Saleh, T. Liloglou, D. J. Rigden, J. L. Parsons, G. J. Grundy, KH-like Domains in PARP9/DTX3L
677 and PARP14 Coordinate Protein-Protein Interactions to Promote Cancer Cell Survival. *J Mol Biol*
678 **436**, 168434 (2024).
679 27. Y. Zhang *et al.*, PARP9-DTX3L ubiquitin ligase targets host histone H2BJ and viral 3C protease to
680 enhance interferon signaling and control viral infection. *Nat Immunol* **16**, 1215-1227 (2015).
681 28. H. Kleine *et al.*, Substrate-assisted catalysis by PARP10 limits its activity to mono-ADP-
682 ribosylation. *Mol Cell* **32**, 57-69 (2008).
683 29. E. Wahlberg *et al.*, Family-wide chemical profiling and structural analysis of PARP and tankyrase
684 inhibitors. *Nat Biotechnol* **30**, 283-288 (2012).
685 30. Z. Wang *et al.*, Recognition of the iso-ADP-ribose moiety in poly(ADP-ribose) by WWE domains
686 suggests a general mechanism for poly(ADP-ribosyl)ation-dependent ubiquitination. *Genes Dev*
687 **26**, 235-240 (2012).
688 31. C. A. Pinkert, *Transgenic Animal Technology: A Laboratory Handbook* (Elsevier Science, 2002).
689 32. H. Miura, R. M. Quadros, C. B. Gurumurthy, M. Ohtsuka, Easi-CRISPR for creating knock-in and
690 conditional knockout mouse models using long ssDNA donors. *Nat Protoc* **13**, 195-215 (2018).
691 33. A. R. Fehr *et al.*, The nsp3 macrodomain promotes virulence in mice with coronavirus-induced
692 encephalitis. *J Virol* **89**, 1523-1536 (2015).
693 34. L. S. Voth *et al.*, Unique Mutations in the Murine Hepatitis Virus Macrodomain Differentially
694 Attenuate Virus Replication, Indicating Multiple Roles for the Macrodomain in Coronavirus
695 Replication. *J Virol* **95**, e0076621 (2021).
696 35. P. A. Schaffer, G. M. Aron, N. Biswal, M. Benyesh-Melnick, Temperature-sensitive mutants of
697 herpes simplex virus type 1: isolation, complementation and partial characterization. *Virology*
698 **52**, 57-71 (1973).
699 36. C. Y. Ly *et al.*, Inhibitors of One or More Cellular Aurora Kinases Impair the Replication of Herpes
700 Simplex Virus 1 and Other DNA and RNA Viruses with Diverse Genomes and Life Cycles.
701 *Microbiol Spectr* **11**, e0194322 (2023).
702 37. S. C. Das, D. Nayak, Y. Zhou, A. K. Pattnaik, Visualization of intracellular transport of vesicular
703 stomatitis virus nucleocapsids in living cells. *J Virol* **80**, 6368-6377 (2006).
704 38. A. J. Hume *et al.*, Recombinant Lloviu virus as a tool to study viral replication and host
705 responses. *PLoS Pathog* **18**, e1010268 (2022).
706 39. J. Olejnik, E. V. Nelson, Analyzing Apoptosis Induction and Evasion in Ebola Virus-Infected Cells.
707 *Methods Mol Biol* **1628**, 227-241 (2017).
708 40. K. M. Rodriguez *et al.*, Chemical genetics and proteome-wide site mapping reveal cysteine
709 MARylation by PARP-7 on immune-relevant protein targets. *eLife* **10**, e60480 (2021).

710 41. J. H. Choi *et al.*, DUSP11-mediated control of 5'-triphosphate RNA regulates RIG-I sensitivity.
711 *Genes Dev* **34**, 1697-1712 (2020).
712 42. P. Bankhead *et al.*, QuPath: Open source software for digital pathology image analysis. *Sci Rep* **7**,
713 16878 (2017).

714

## FIGURE LEGENDS

**Fig. 1. PARP14 promotes IFN production following poly(I:C) treatment in human A549 cells.** A-B) WT (red bars) and PARP14 knock-out (KO) (green bars) A549 cells were transfected with 0.5ug/mL poly(I:C), RNA was isolated from cells at 18 hours post-tranfection (hpt) and IFNβ (A) and IFNλ (B) mRNA levels were quantified by qPCR using ΔCt method. C-D) WT and PARP14 KO cells were transfected with 0.5μg/mL poly(I:C). Supernatant was collected 18 hpt and IFNβ (C) and IFNλ (D) protein levels were quantified by ELISA. Data shown in A-D are from 1 experiment and are representative of 3 independent experiments with N=3 for each experiment. E) WT and PARP14 KO cells were either mock transfected or transfected with 0.5 μg/mL of poly(I:C). Cell lysates were collected at 18 hpt and OAS3 and PARP14 protein levels were determined by immunoblotting using β-actin as a loading control. F) Band intensities from E were quantified by densitometry, normalized to β-actin, and then relative levels as compared to mock transfected WT cells were determined. Data shown in E-F are from 1 experiment and are representative of 3 independent experiments with N=1 for each experiment. G) WT cells were either mock transfected or transfected with 0.5 μg/mL of poly(I:C) and were immediately either treated with DMSO (vehicle) or with increasing concentrations of PARP14i (0.01, 0.1, and 1 μM). At 18 hpt RNA was isolated from cells and IFNβ mRNA was quantified by qPCR using ΔCt method. H) WT A549 cells transfected with poly(I:C) were treated with 1 μM PARP14 Degron control (CTL) or PARP14 Degron (DEG) for 18 hours. RNA was isolated from cells at 18 hpt and IFNβ mRNA was quantified by qPCR using ΔCt method. I) WT and PARP14 KO cells were transfected with 0.5 μg of YFP or YFP-PARP14 plasmids. At 48 hpt cells were transfected with 0.5 μg/mL of poly(I:C) and 18 hours later RNA was isolated from cells and IFNβ mRNA was quantified by qPCR using

ΔCt method. Data shown in G-I are from 1 experiment and are representative of 3 independent experiments with N=3 for each experiment.

**Fig. 2. PARP14 promotes IFN production following Mac1 mutant CoV infection.** A) Schematic diagram showing the generation of PARP14 KO mice for Bone-marrow cell isolation. Parp14 floxed mice were crossed with cre heterozygote mice and the resulting progeny were used to harvest bone marrow. Bone marrow cells were isolated and plated with 10ng/mL of mCSF or GM-CSF for 6 days to differentiate cells into M0 macrophages or dendritic cells (DCs), respectively. On day 6, these cells were treated with 1μg/mL of 4-hydroxy tamoxifen (4-OHT) for 24 hours to induce Cre expression leading to the removal of exon 2 of Parp14 (for details see Methods). B-C) Parp14+/+ (Cre-) (red bars) and Parp14-/- (Cre+) (green bars) M0 cells (B) or DCs (C) were infected with MHV WT (solid bars) and N1347A (checkered bars) at an MOI of 0.1. RNA was isolated from cells at 12 hpi and IFNβ mRNA was quantified by qPCR using ΔCt method. D) Parp14+/+ cells were infected with WT and N1347A at an MOI of 0.1 and then treated at 1 hpi with DMSO or increasing concentrations of PARP14 inhibitor (PARP14i) (3, 11, 33, 99 and 297nM). RNA was isolated from cells at 12 hpi and IFNβ mRNA levels were quantified using qPCR using ΔCt method. E) Parp14+/+ and Parp14-/- M0 macrophages were infected with WT and N1347A MHV at an MOI of 0.1 and then treated with DMSO or 100 nM PARP14i at 1 hpi. The cell supernatant was collected at 12 hpi and IFNβ protein was quantified by ELISA. F) A549-ACE2 cells were infected with WT and ΔMac1 SARS-COV-2 at an MOI of 0.1 and treated with DMSO or PARP14i. RNA was isolated from cells at 48 hpi and IFNβ, IFNλ and CXCL10 mRNA levels were quantified by qPCR using ΔCt method. Data shown in B-F are

from 1 experiment and are representative of 3 independent experiments with N=3 for each experiment.

**Fig. 3. PARP14 regulates the transcription of dozens of genes with multiple biological functions following MHV-N1347A infection of BMDMs.** A) WT BMDMs were infected with N1347A MHV at an MOI of 0.1 and then treated with DMSO or 100 nM PARP14i at 1 hpi. RNA was collected from these cells at 12 hpi and RNAseq was performed to quantify the transcriptome with and without PARP14i. The ratio of gene expression in the presence or absence of PARP14i treatment was plotted against minus $\log_{10}$ value of the p-adjusted value as a volcano plot. B) Gene ontology analysis/pathway enrichment analysis of genes that were identified to be promoted by PARP14 catalytic activity carried out using DAVID gene ontology tool. Pathways enriched with a p-value of less that 0.05 were plotted. C) WT BMDMs were infected with MHV N1347A at an MOI of 0.1 and treated with DMSO or 100 nM PARP14i at 1 hpi. RNA was isolated from cells at 12 hpi and CASP1, FOXO3 and RNF111 mRNAs were quantified by qPCR using ΔCt method. RNAseq data shown in A-B are from 1 experiment with N=3. Data shown in C are from 1 experiment and are representative of 2 independent experiments with N=3 for each experiment.

**Fig. 4. PARP14 inhibits the replication of Mac1-mutant MHV and SARS-CoV-2.** A) *Parp14* floxed *cre+/-* BMDMs were treated with and without 4-OHT. 24 hours later these cells were infected with WT and N1347A MHV at an MOI of 0.1. At 20 hpi cells and supernatants were collected and progeny virus was quantified by plaque assay. B-C) PARP14 floxed *cre+* BMDMs (B) and DCs (C) were treated with or without 4-OHT. 24 hours later these cells were infected with WT and N1347A MHV at an MOI of 0.1. At 20 hpi cells and supernatants were collected and progeny virus was quantified by plaque assay. Data shown in

A-C are from 1 experiment and are representative of 3 independent experiments with N=3 for each experiment. D) PARP14$^{+/+}$ BMDMs and DCs were infected with WT and N1347A MHV at an MOI of 0.1 and then treated with DMSO or PARP14i (1 $\mu$M). At 20hpi cells and supernatants were collected and progeny virus was quantified by plaque assay. Data shown in D are from 1 experiment and are representative of 3 independent experiments with N=4 for each experiment. E) WT Calu-3 cells were either mock-treated or IFN$\gamma$-treated (50 Units) O/N. These cells were then infected with WT and $\Delta$Mac1 SARS-COV-2 at an MOI of 0.1 and treated with DMSO or PARP14i (1 $\mu$M) at 1 hpi. At 48 hpi cells and supernatants were collected and progeny virus was quantified by plaque assay. Data shown in E are from 1 experiment and are representative of 3 independent experiments with N=3 for each experiment.

**Fig. 5. PARP14 restricts the replication of HSV-1 in A549 cells.** A) WT and PARP14 KO A549 cells were infected with HSV-1 at an MOI of 0.01 PFU/cell. Cells and supernatants were collected at indicated time points and progeny virus was quantified by plaque assay. B) WT and PARP14 KO A549 cells were infected with HSV-1 at an MOI of 0.1. At 24 hpi RNA was harvested from infected cells and HSV-1 immediate early gene ICP4, ICP0 and ICP27 mRNAs were quantified by qPCR using $\Delta$Ct method having 18S rRNA abundance as the endogenous control. The data in A-B is from 1 experiment representative of 2 independent experiments. N=3 per group. C) WT and PARP14 KO A549 cells were infected with serial dilutions of HSV-1 starting at a concentration of $1.85\times10^9$ PFU/ml and plaquing efficiency was determined at 24 hpi. This data is the combined results of 3 separate experiments, N=9 per group. D) WT A549 cells were infected with HSV-1 at an MOI of 0.1 PFU/cell and then treated with DMSO or PARP14i (1 $\mu$M) at 1 hpi. Cells and supernatants

were collected at 24 hpi and progeny virus was quantified by plaque assay. The data in D is from 1 experiment representative of 2 independent experiments. N=3 per group.

**Fig. 6. PARP14 is required for the replication of VSV-GFP, EBOV-ZsGreen and NiV in cell culture.** A) A549 WT and PARP14 KO cells were infected with VSV-GFP at 1 MOI. At 8hpi, cells and supernatants were collected and progeny virus was quantified by $TCID_{50}$. Results in A are from one experiment representative of 3 independent experiments. n=3. B-C) A549 WT and PARP14 KO cells were infected with rEBOV-ZsG-P2A-VP40 (rEBOV-ZsG) at an MOI of 10. At 48hpi, cells were fixed with 10% formalin and imaged following nuclear staining (B). Relative infection rate of rEBOV-ZsG was determined by QuPath software using the Positive Cell Detection function using ZsGreen fluorescence intensity in the area surrounding each detected nucleus to identify positive cells (C). D) A549 WT and PARP14 KO cells were infected with NiV-Bangladesh strain (NiV-B) at an MOI of 10. At 48 hpi, cells were fixed with 10% formalin and stained with $\alpha$-NiV-B antibody and then with a AlexaFluor 488 conjugated secondary antibody. Cells were then imaged following nuclear staining. Relative infection rate was determined as described in C using QuPath to detect AF488 staining. E) A549 WT cells were infected with rEBOV-ZsG at an MOI of 10 and then treated with DMSO or 100 nM PARP14i (P14i) at 1 hpi. At 48hpi, cells were fixed with 10% formalin and imaged following nuclear staining. Relative infection rate was quantified by QuPath as described in C. F) A549 WT cells were infected with NiV-B at an MOI of 10. At 48 hpi, cells were fixed with 10% formalin and stained with $\alpha$-NiV-B antibody and then with a AlexaFluor 488 conjugated secondary antibody. Cells were then imaged following nuclear staining. Relative infection rate was determined as described in D using QuPath to detect

AF488 staining. The data in C-F are the combined results of 3 independent experiments. C-D N=10 per group; E-F N=9 per group.

**Fig. S1.** A) WT and PARP14 KO NHDF cells were transfected with 0.5μg/mL poly(I:C), at 18 hpt RNA was isolated from cells and the level of IFNβ mRNA was quantified using qPCR using ΔCt method. Data shown in A are from 1 experiment and are representative of 3 independent experiments with N=3 for each experiment. B) 293T cells were mock transfected (M) or transfected with plasmid expressing GFP-PARP14 G832E. At 24 hpt, cells were treated with PARPi for 4 hrs. Cells were then collected and analyzed by immunoblot with indicated antibodies. Data shown in B are from 1 experiment representative of 2 independent experiments. C) A549 WT cells were treated with either DMSO, negative control (CTL) or PARP14 Degron (DEG) for 6 hrs and then wither mock transfected or transfected with 0.5μg/mL of poly(I:C) with the corresponding treatments. At 18 hpt cell lysates were collected and PARP14 protein levels were determined by immunoblotting using β-actin as a loading control.

**Fig. S2.** A) Floxed Parp14 *cre-* (*Parp14+/+*) and *cre+* (*Parp14-/-*) BMDMs were treated with 4-OHT and 24 hours later were infected with MHV WT and N1347A at an MOI of 0.1. At 12hpi, cell lysates were harvested and levels of PARP14 and β-actin were determined by immunoblotting. B) *Parp14+/+* and *Parp14-/-* BMDMs were infected with WT and N1347A MHV-JHM at an MOI of 0.1. RNA was collected 12 hpi and ISG15 mRNA levels were quantified using qPCR using ΔCt method. C) RNA was isolated from BMDMs and DCs and CXCR1 mRNA levels were quantified using qPCR using ΔCt method. Data shown in A are from 1 experiment and are representative of 3 independent experiments with N=1 for each

experiment. Data shown in B-C are from 1 experiment and are representative of 3 independent experiments with N=3 for each experiment.

**Fig. S3. PARP14 restricts the replication of HSV-1 in A549 cells.** WT and PARP14 KO A549 cells were infected with HSV-1 at an MOI of 0.01 PFU/cell. At 1 hpi cells were treated with 1 μM PARP14 Degron control (CTL) or PARP14 Degron (DEG). At 24 hpi RNA was harvested from infected cells and HSV-1 immediate early gene ICP4, ICP0 and ICP27 mRNAs were quantified by qPCR using ΔCt method having 18S rRNA abundance as the endogenous control. The data is from 1 experiment representative of 2 independent experiments. N=3 per group

**Fig. S4. PARP14 does not impact LCMV infection.** A) Gating strategy used to identify $LCMV^{cl13}$(+) cells by flow cytometry. B) WT and PARP14 KO BMDMs were infected with $LCMV^{cl13}$ at an MOI of 1 and the % of $LCMV^{cl13}$ (+) cells were quantified by flow cytometry. These data are from 1 experiment representative of 3 independent experiments. N=3 per group.

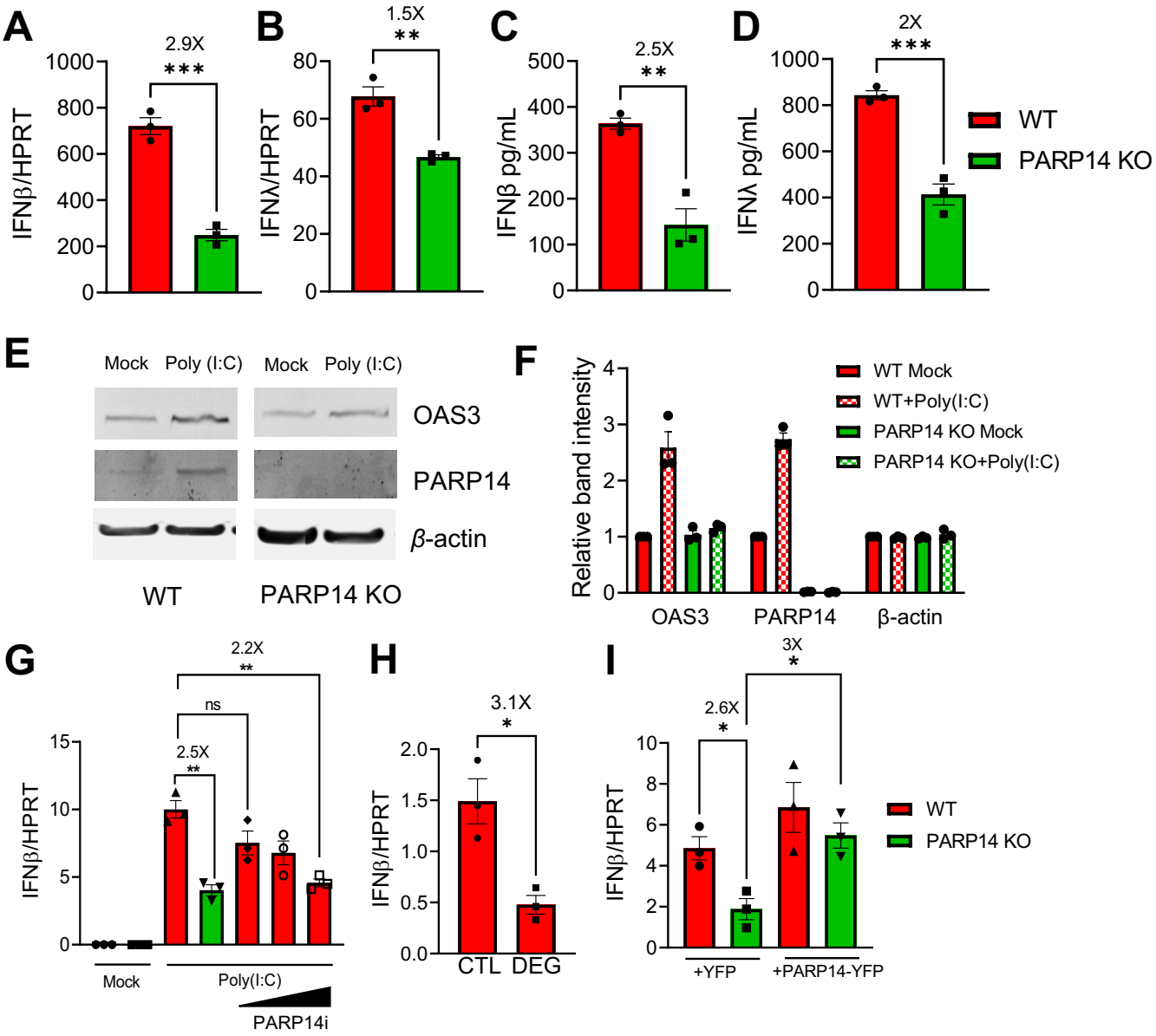
A
2.9X
***
IFNβ/HPRT
1000
800
600
400
200
0
B
1.5X
**
IFNλ/HPRT
80
60
40
20
0
C
2.5X
**
IFNβ pg/mL
500
400
300
200
100
0
D
2X
***
IFNλ pg/mL
1000
800
600
400
200
0
WT
PARP14 KO
E
Mock
Poly (I:C)
Mock
Poly (I:C)
OAS3
PARP14
β-actin
WT
PARP14 KO
F
Relative band intensity
4
3
2
1
0
WT Mock
WT+Poly(I:C)
PARP14 KO Mock
PARP14 KO+Poly(I:C)
OAS3
PARP14
β-actin
G
2.2X
**
ns
2.5X
**
IFNβ/HPRT
15
10
5
0
Mock
Poly(I:C)
PARP14i
H
3.1X
*
IFNβ/HPRT
2.0
1.5
1.0
0.5
0.0
CTL
DEG
I
3X
*
2.6X
*
IFNβ/HPRT
10
8
6
4
2
0
WT
PARP14 KO
+YFP
+PARP14-YFP

**Fig. 1. PARP14 promotes IFN production following poly(I:C) treatment in human A549 cells.** A-B) WT (red bars) and PARP14 knock-out (KO) (green bars) A549 cells were transfected with 0.5ug/mL poly(I:C), RNA was isolated from cells at 18 hours post-tranfection (hpt) and IFNβ (A) and IFNλ (B) mRNA levels were quantified by qPCR using ΔCt method. C-D) WT and PARP14 KO cells were transfected with 0.5μg/mL poly(I:C). Supernatant was collected 18 hpt and IFNβ (C) and IFNλ (D) protein levels were quantified by ELISA. Data shown in A-D are from 1 experiment and are representative of 3 independent experiments with N=3 for each experiment. E) WT and PARP14 KO cells were either mock transfected or transfected with 0.5 μg/mL of poly(I:C). Cell lysates were collected at 18 hpt and OAS3 and PARP14 protein levels were determined by immunoblotting using β-actin as a loading control. F) Band intensities from E were quantified by densitometry, normalized to β-actin, and then relative levels as compared to mock transfected WT cells were determined. Data shown in E-F are from 1 experiment and are representative of 3 independent experiments with N=1 for each experiment. G) WT cells were either mock transfected or transfected with 0.5 μg/mL of poly(I:C) and were immediately either treated with DMSO (vehicle) or with increasing concentrations of PARP14i (0.01, 0.1, and 1 μM). At 18 hpt RNA was isolated from cells and IFNβ mRNA was quantified by qPCR using ΔCt method. H) WT A549 cells transfected with poly(I:C) were treated with 1 μM PARP14 Degron control (CTL) or PARP14 Degron (DEG) for 18 hours. RNA was isolated from cells at 18 hpt and IFNβ mRNA was quantified by qPCR using ΔCt method. I) WT and PARP14 KO cells were transfected with 0.5 μg of YFP or YFP-PARP14 plasmids. At 48 hpt cells were transfected with 0.5 μg/mL of poly(I:C) and 18 hours later RNA was isolated from cells and IFNβ mRNA was quantified by qPCR using ΔCt method. Data shown in G-I are from 1 experiment and are representative of 3 independent experiments with N=3 for each experiment.

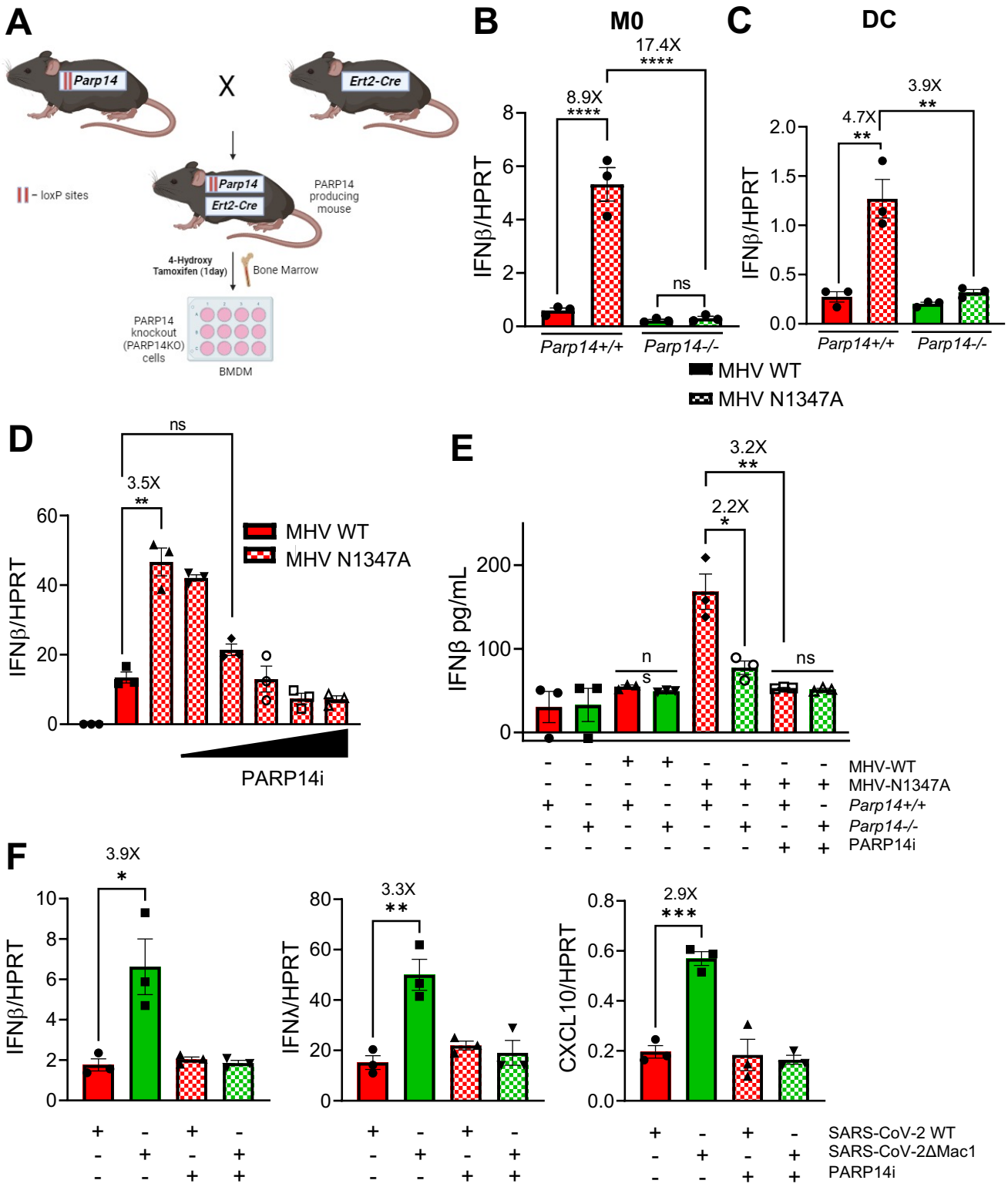
A
Parp14
X
Ert2-Cre
loxP sites
Parp14
Ert2-Cre
PARP14 producing mouse
4-Hydroxy Tamoxifen (1day)
Bone Marrow
PARP14 knockout (PARP14KO) cells
BMDM
B
M0
17.4X
****
8.9X
****
ns
IFNβ/HPRT
Parp14+/+
Parp14-/-
C
DC
3.9X
**
4.7X
**
IFNβ/HPRT
Parp14+/+
Parp14-/-
MHV WT
MHV N1347A
D
ns
3.5X
**
IFNβ/HPRT
MHV WT
MHV N1347A
PARP14i
E
3.2X
**
2.2X
*
IFNβ pg/mL
ns
ns
MHV-WT
MHV-N1347A
Parp14+/+
Parp14-/-
PARP14i
F
3.9X
*
IFNβ/HPRT
3.3X
**
IFNλ/HPRT
2.9X
***
CXCL10/HPRT
SARS-CoV-2 WT
SARS-CoV-2ΔMac1
PARP14i

**Fig. 2. PARP14 promotes IFN production following Mac1 mutant CoV infection.** A) Schematic diagram showing the generation of PARP14 KO mice for Bone-marrow cell isolation. *Parp14* floxed mice were crossed with *cre* heterozygote mice and the resulting progeny were used to harvest bone marrow. Bone marrow cells were isolated and plated with 10ng/mL of mCSF or GM-CSF for 6 days to differentiate cells into M0 macrophages or dendritic cells (DCs), respectively. On day 6, these cells were treated with 1µg/mL of 4-hydroxy tamoxifen (4-OHT) for 24 hours to induce *Cre* expression leading to the removal of exon 2 of *Parp14* (for details see Methods). B-C) *Parp14+/+* (Cre-) (red bars) and *Parp14-/-* (Cre+) (green bars) M0 cells (B) or DCs (C) were infected with MHV WT (solid bars) and N1347A (checkered bars) at an MOI of 0.1. RNA was isolated from cells at 12 hpi and IFNβ mRNA was quantified by qPCR using ΔCt method. D) *Parp14+/+* cells were infected with WT and N1347A at an MOI of 0.1 and then treated at 1 hpi with DMSO or increasing concentrations of PARP14 inhibitor (PARP14i) (3, 11, 33, 99 and 297nM). RNA was isolated from cells at 12 hpi and IFNβ mRNA levels were quantified using qPCR using ΔCt method. E) *Parp14+/+* and *Parp14-/-* M0 macrophages were infected with WT and N1347A MHV at an MOI of 0.1 and then treated with DMSO or 100 nM PARP14i at 1 hpi. The cell supernatant was collected at 12 hpi and IFNβ protein was quantified by ELISA. F) A549-ACE2 cells were infected with WT and ⊿Mac1 SARS-COV-2 at an MOI of 0.1 and treated with DMSO or PARP14i. RNA was isolated from cells at 48 hpi and IFNβ, IFNλ and CXCL10 mRNA levels were quantified by qPCR using ΔCt method. Data shown in B-F are from 1 experiment and are representative of 3 independent experiments with N=3 for each experiment.

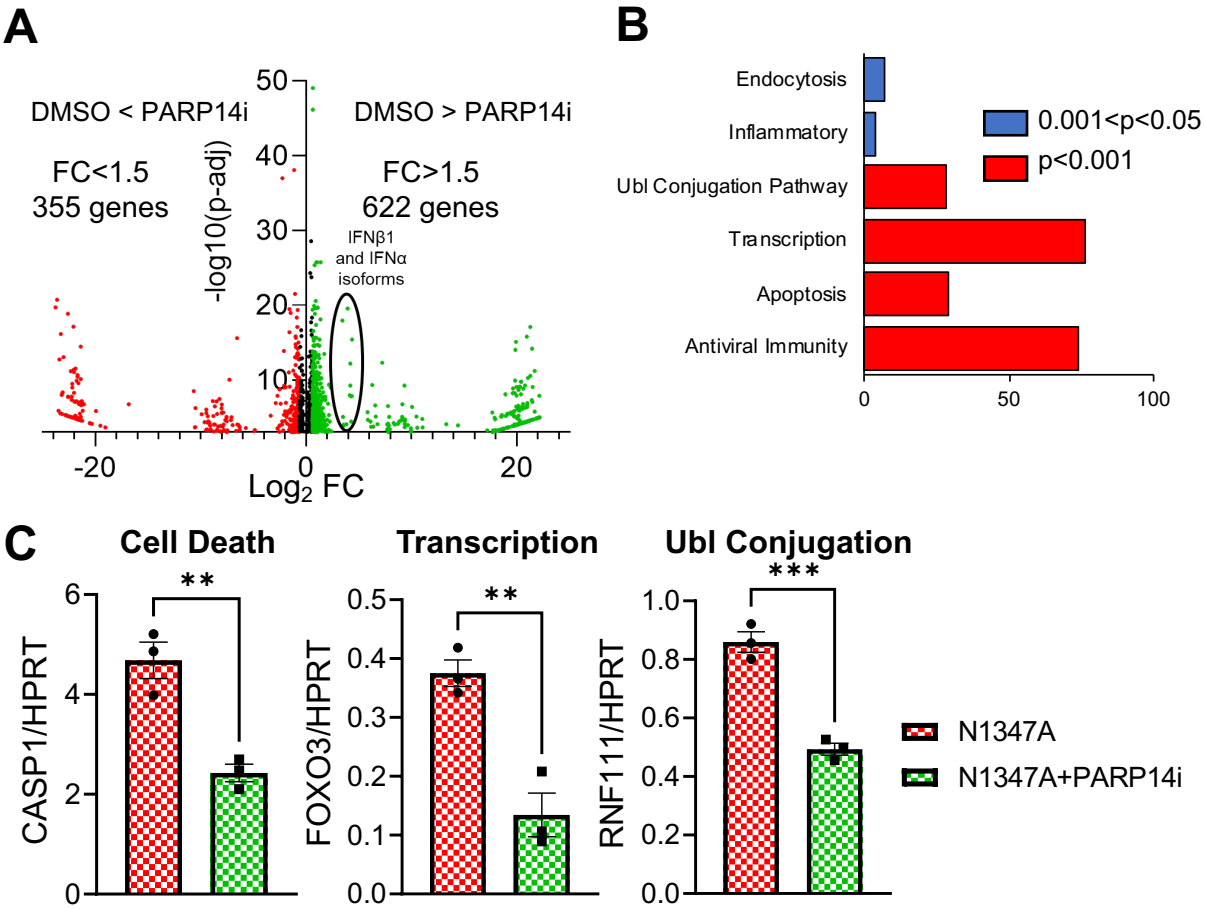


**Fig. 3. PARP14 regulates the transcription of dozens of genes with multiple biological functions following MHV-N1347A infection of BMDMs.** A) WT BMDMs were infected with N1347A MHV at an MOI of 0.1 and then treated with DMSO or 100 nM PARP14i at 1 hpi. RNA was collected from these cells at 12 hpi and RNAseq was performed to quantify the transcriptome with and without PARP14i. The ratio of gene expression in the presence or absence of PARP14i treatment was plotted against minus $\log_{10}$ value of the p-adjusted value as a volcano plot. B) Gene ontology analysis/pathway enrichment analysis of genes that were identified to be promoted by PARP14 catalytic activity carried out using DAVID gene ontology tool. Pathways enriched with a p-value of less that 0.05 were plotted. C) WT BMDMs were infected with MHV N1347A at an MOI of 0.1 and treated with DMSO or 100 nM PARP14i at 1 hpi. RNA was isolated from cells at 12 hpi and CASP1, FOXO3 and RNF111 mRNAs were quantified by qPCR using ΔCt method. RNAseq data shown in A-B are from 1 experiment with N=3. Data shown in C are from 1 experiment and are representative of 2 independent experiments with N=3 for each experiment.

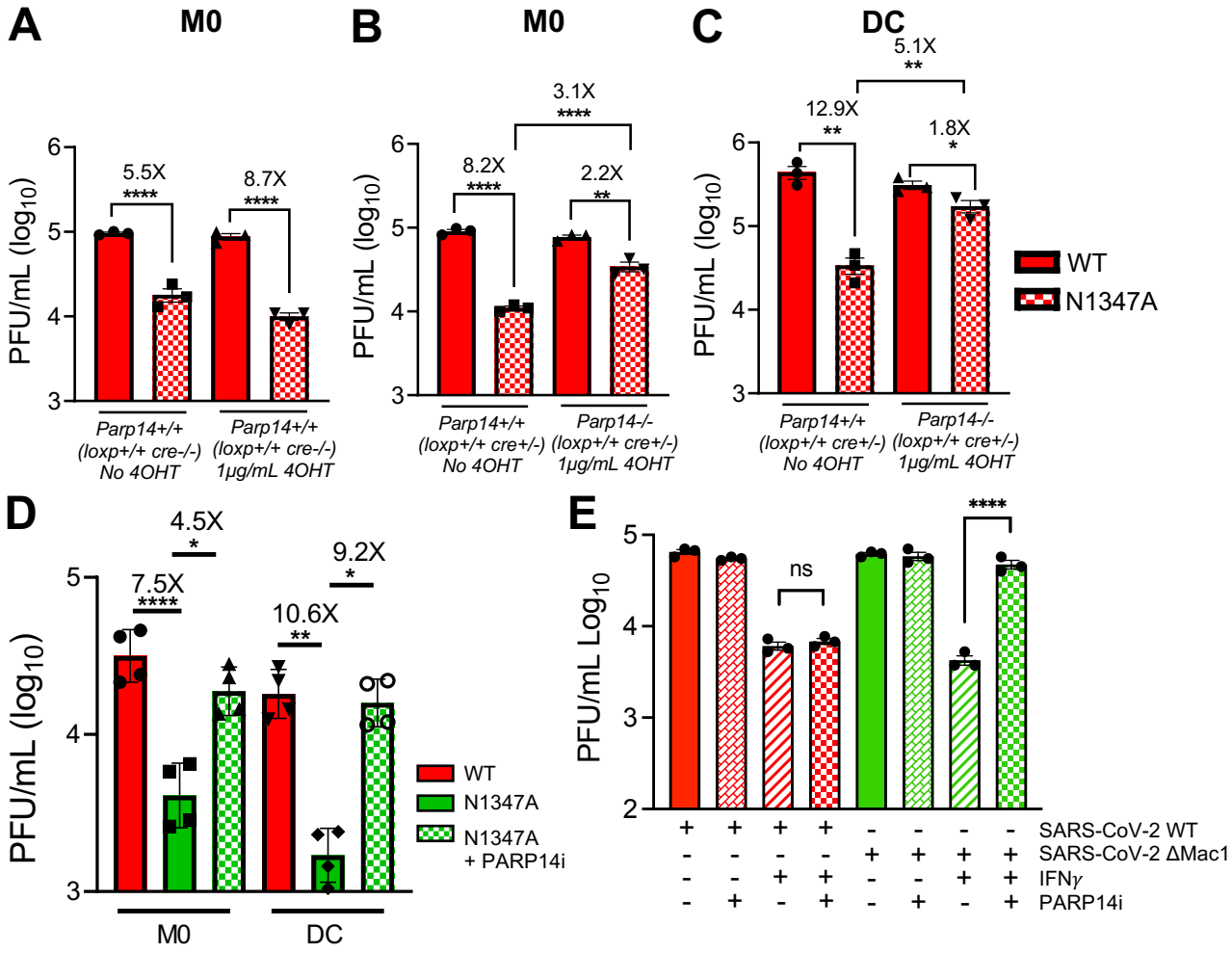


**Fig. 4. PARP14 inhibits the replication of Mac1-mutant MHV and SARS-CoV-2.** A) *Parp14* floxed *cre+/-* BMDMs were treated with and without 4-OHT. 24 hours later these cells were infected with WT and N1347A MHV at an MOI of 0.1. At 20 hpi cells and supernatants were collected and progeny virus was quantified by plaque assay. B-C) PARP14 floxed *cre+* BMDMs (B) and DCs (C) were treated with or without 4-OHT. 24 hours later these cells were infected with WT and N1347A MHV at an MOI of 0.1. At 20 hpi cells and supernatants were collected and progeny virus was quantified by plaque assay. Data shown in A-C are from 1 experiment and are representative of 3 independent experiments with N=3 for each experiment. D) PARP14$^{+/+}$ BMDMs and DCs were infected with WT and N1347A MHV at an MOI of 0.1 and then treated with DMSO or PARP14i (1 $\mu$M). At 20hpi cells and supernatants were collected and progeny virus was quantified by plaque assay. Data shown in D are from 1 experiment and are representative of 3 independent experiments with N=4 for each experiment. E) WT Calu-3 cells were either mock-treated or IFN$\gamma$-treated (50 Units) O/N. These cells were then infected with WT and $\Delta$Mac1 SARS-COV-2 at an MOI of 0.1 and treated with DMSO or PARP14i (1 $\mu$M) at 1 hpi. At 48 hpi cells and supernatants were collected and progeny virus was quantified by plaque assay. Data shown in E are from 1 experiment and are representative of 3 independent experiments with N=3 for each experiment.

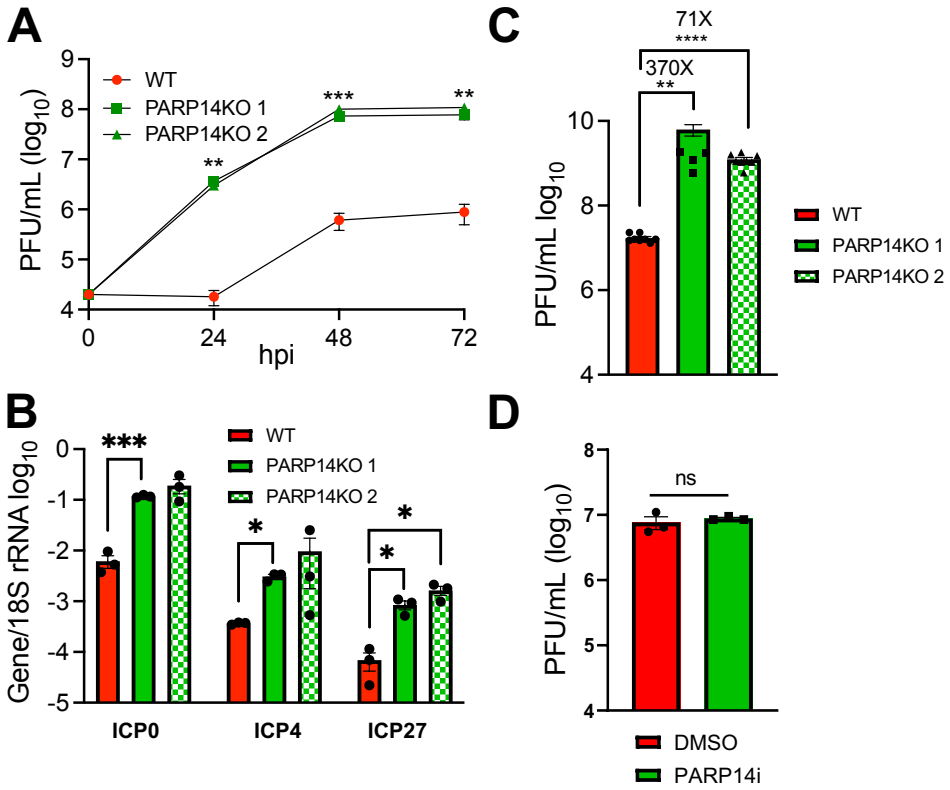


**Fig. 5. PARP14 restricts the replication of HSV-1 in A549 cells.** A) WT and PARP14 KO A549 cells were infected with HSV-1 at an MOI of 0.01 PFU/cell. Cells and supernatants were collected at indicated time points and progeny virus was quantified by plaque assay. B) WT and PARP14 KO A549 cells were infected with HSV-1 at an MOI of 0.1. At 24 hpi RNA was harvested from infected cells and HSV-1 immediate early gene ICP4, ICP0 and ICP27 mRNAs were quantified by qPCR using ΔCt method having 18S rRNA abundance as the endogenous control. The data in A-B is from 1 experiment representative of 2 independent experiments. N=3 per group. C) WT and PARP14 KO A549 cells were infected with serial dilutions of HSV-1 starting at a concentration of $1.85\times10^9$ PFU/ml and plaquing efficiency was determined at 24 hpi. This data is the combined results of 3 separate experiments, N=9 per group. D) WT A549 cells were infected with HSV-1 at an MOI of 0.1 PFU/cell and then treated with DMSO or PARP14i (1 $\mu$M) at 1 hpi. Cells and supernatants were collected at 24 hpi and progeny virus was quantified by plaque assay. The data in D is from 1 experiment representative of 2 independent experiments. N=3 per group.

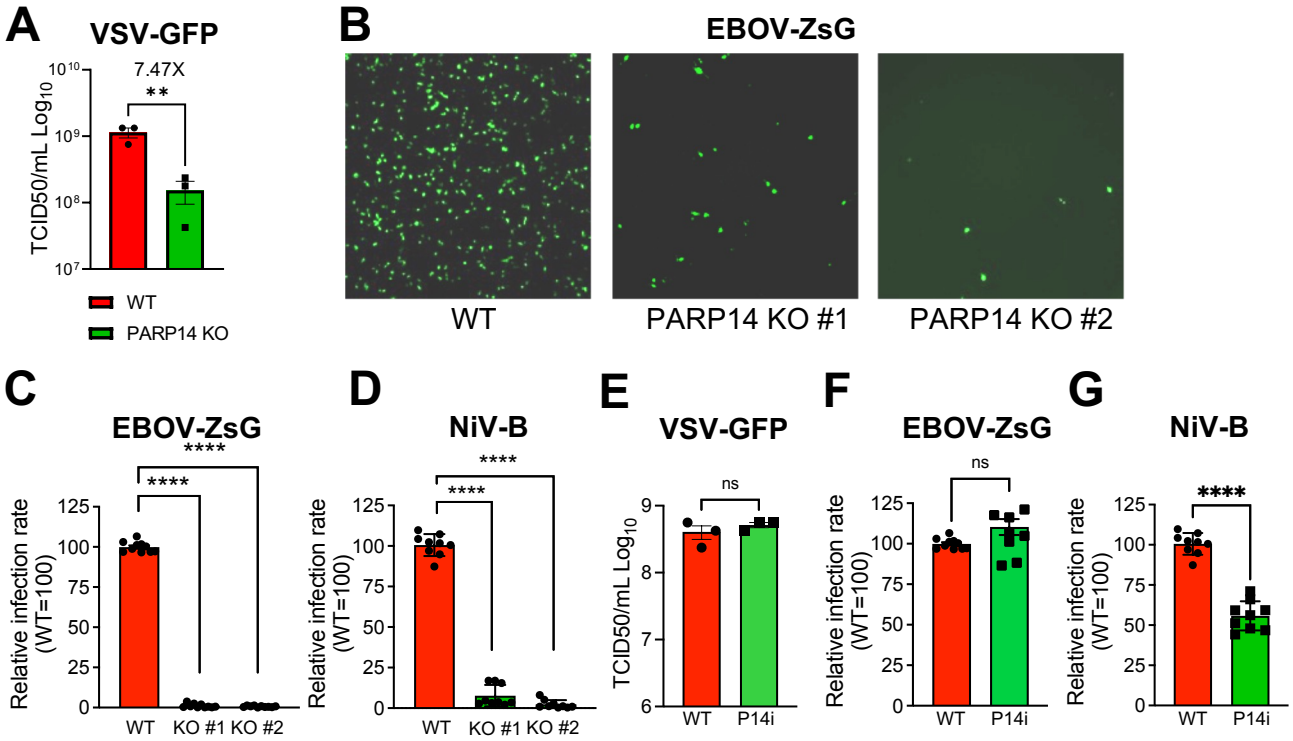


**Fig. 6. PARP14 is required for the replication of VSV-GFP, EBOV-ZsGreen and NiV in cell culture.** A) A549 WT and PARP14 KO cells were infected with VSV-GFP at 1 MOI. At 8hpi, cells and supernatants were collected and progeny virus was quantified by $TCID_{50}$. Results in A are from one experiment representative of 3 independent experiments. n=3. B-C) A549 WT and PARP14 KO cells were infected with rEBOV-ZsG-P2A-VP40 (rEBOV-ZsG) at an MOI of 10. At 48hpi, cells were fixed with 10% formalin and imaged following nuclear staining (B). Relative infection rate of rEBOV-ZsG was determined by QuPath software using the Positive Cell Detection function using ZsGreen fluorescence intensity in the area surrounding each detected nucleus to identify positive cells (C). D) A549 WT and PARP14 KO cells were infected with NiV-Bangladesh strain (NiV-B) at an MOI of 10. At 48 hpi, cells were fixed with 10% formalin and stained with $\alpha$-NiV-B antibody and then with a AlexaFluor 488 conjugated secondary antibody. Cells were then imaged following nuclear staining. Relative infection rate was determined as described in C using QuPath to detect AF488 staining. E) A549 WT cells were infected with rEBOV-ZsG at an MOI of 10 and then treated with DMSO or 100 nM PARP14i (P14i) at 1 hpi. At 48hpi, cells were fixed with 10% formalin and imaged following nuclear staining. Relative infection rate was quantified by QuPath as described in C. F) A549 WT cells were infected with NiV-B at an MOI of 10. At 48 hpi, cells were fixed with 10% formalin and stained with $\alpha$-NiV-B antibody and then with a AlexaFluor 488 conjugated secondary antibody. Cells were then imaged following nuclear staining. Relative infection rate was determined as described in D using QuPath to detect AF488 staining. The data in C-F are the combined results of 3 independent experiments. C-D N=10 per group; E-F N=9 per group.